OPEN ACCESS Freely available online

PLOS ONE

Regulation of Ion Gradients across Myocardial Ischemic Border Zones: A Biophysical Modelling Analysis

Steven Niederer*

Biomedical Engineering, King's College London, London, United Kingdom

Abstract

The myocardial ischemic border zone is associated with the initiation and sustenance of arrhythmias. The profile of ionic concentrations across the border zone play a significant role in determining cellular electrophysiology and conductivity, yet their spatial-temporal evolution and regulation are not well understood. To investigate the changes in ion concentrations that regulate cellular electrophysiology, a mathematical model of ion movement in the intra and extracellular space in the presence of ionic, potential and material property heterogeneities was developed. The model simulates the spatial and temporal evolution of concentrations of potassium, sodium, chloride, calcium, hydrogen and bicarbonate ions and carbon dioxide across an ischemic border zone. Ischemia was simulated by sodium-potassium pump inhibition, potassium channel activation and respiratory and metabolic acidosis. The model predicted significant disparities in the width of the border zone for each ionic species, with intracellular sodium and extracellular potassium having discordant gradients, facilitating multiple gradients in cellular properties across the border zone. Extracellular potassium was found to have the largest border zone and this was attributed to the voltage dependence of the potassium channels. The model also predicted the efflux of K^+ from the ischemic region due to electrogenic drift and diffusion within the intra and extracellular space, respectively, which contributed to K^+ depletion in the ischemic region.

Citation: Niederer S (2013) Regulation of Ion Gradients across Myocardial Ischemic Border Zones: A Biophysical Modelling Analysis. PLoS ONE 8(4): e60323. doi:10.1371/journal.pone.0060323

Editor: Vladimir E. Bondarenko, Georgia State University, United States of America

Received November 5, 2012; **Accepted** February 24, 2013; **Published** April 5, 2013

Funding: The work was supported by UK Engineering and Physical Sciences Research Council EP/F043929/1, British Heart Foundation (PG/11/101/29212) and Boston Scientific. The funders had no role in study design, data collection and analysis, decision to publish, or preparation of the manuscript.

Competing Interests: The author has the following interests. This study was partly funded by Boston Scientific. There are no patents, products in development or marketed products to declare. This does not alter the author's adherence to all the PLOS ONE policies on sharing data and materials, as detailed online in the guide for authors.

* E-mail: steven.niederer@kcl.ac.uk

Introduction

Myocardial ischemia is caused by reduced perfusion to regions of the heart leading to a localised reduction in supply of metabolites, limited waste removal and compromised ionic homeostasis. The first 10 minutes of ischemia are associated with an increased risk of arrhythmias peaking after 5–6 minutes [1]. During this period arrhythmias are commonly initiated within the border zone (BZ) separating viable, well perfused, tissue and the ischemic, underperfused, region [2–4]. Ischemia causes an increase in extracellular potassium ($[K^+]_e$), intra and extracellular proton concentrations ($[H^+]_i$ and $[H^+]_e$, respectively), intracellular sodium ($[Na^+]_i$) and intracellular calcium ($[Ca^{2+}]_i$) concentrations [5]. The dominant mechanisms for these changes have been attributed to a shift in the ATP/ADP ratio, which inhibits the Sodium-Potassium ATPase pump (NaK) and increases the conductance of ATP-inactivated K^+ channels; respiratory acidosis causing an increase in CO_2; and metabolic acidosis, where a shift towards anaerobic respiration increases the production of H^+ in the cell [5]. Inherently, these changes in ionic concentrations in the ischemic region lead to gradients in properties across the BZ, creating electrophysiological heterogeneities that are thought to favour the occurrence of arrhythmias [6–8].

Experimentally, the development of gradients of extracellular pH (pH_e) and $[K^+]_e$ [9,10] have been well characterised using ion sensitive electrodes. Intracellular metabolite gradients have been characterised by fluorescent NADH [11] and biopsy [12] measurements. However, less is known on the gradients of intracellular ions, in particular $[Na^+]_i$, $[Ca^{2+}]_i$ and $[H^+]_i$, nor are the mechanisms that underpin the spatial and temporal evolution of these ion concentration gradients well characterised or understood. This study aims to investigate the spatial-temporal evolution of ion gradients across ischemic BZ and the primary regulators of the BZ size and rate of development.

Previous measurements of ion concentrations and metabolites across the BZ have either been performed at multiple locations but at a limited number of time points [10,12] or have tracked the time evolution of ion concentrations but only from a limited number of locations [13,14]. Furthermore, these measurements have only been able to characterise a subset of ions of interest across the BZ. The need to track the evolution of multiple ionic species in space and time to understand the gradients of cellular electrophysiology across the BZ motivates the use of biophysical computational modelling. Previous models of electrophysiology during acute regional ischemia have simulated the effects of these spatial gradients but have not simulated their time evolution [15–17]. More recent work has simulated the time evolution of $[K^+]_e$ gradients [18], but have not considered other ionic gradients, the effects of nonlinear interactions between K^+ and other ions, the effect of K^+ diffusion in the intracellular space or the effects of potential gradients on ion diffusion.

In this study a new model of cardiac tissue electrophysiology is developed to investigate the spatial-temporal evolution of ionic concentrations across the ischemic BZ, during the first 5 minutes of reduced perfusion. The proposed model extends the conventional bidomain equations to explicitly link membrane potential to ionic concentrations and enforces ionic species conservation. A model of ion regulation across the cell membrane is then developed, parameterized, validated and coupled to the tissue model. This combined model is then used to investigate the spatial and temporal dispersion of ions across the BZ.

Methods

To model the evolution of ionic concentrations in the presence of multiple ionic gradients, electric gradients and heterogeneous tissue properties requires the development of a new set of equations for modelling the myocardium. In the next section the equations to model the BZ are derived and a model of passive cell membrane ion regulation is developed and validated. The changes to the cell membrane model to simulate *NaK* inhibition, K^+ channel activation, respiratory acidosis and metabolic acidosis are then described.

Tissue Model Derivation

Consistent with previous models of cardiac tissue electrophysiology the myocardium is represented as a two phase medium, with each point in the domain containing a fraction of intra and extracellular space. This gives rise to the scaling variables.

$$\alpha_x = \frac{\Omega_x}{\Omega} \quad \chi = \frac{\Gamma}{\Omega} \tag{1}$$

where Ω_x is the volume of the x space in a unit of Ω myocardium volume, α_x is the volume fraction of space x (with x corresponding to the extra (e) or intra (i) cellular space), χ is the interspace surface area per unit volume myocardium and Γ is area of the interspace surface. The intracellular volume fraction (α_i) can be separated into sub volume fractions representing the cytosol (α_{cyt}), mitochondria (α_{mito}) or the sarcoplasmic reticulum (α_{SR}) to model distinct subcellular spaces, as described below. At each point in space there exists an intracellular potential (ϕ_i), an extracellular potential (ϕ_e), a transmembrane potential (V_m) and an intra and extracellular ion concentration for each of the ion species in the model. The movement of each ion species in each domain is driven by diffusion, due to a gradient in ion concentration, and drift, due to a gradient in the electric field. This movement is described by the Nernst-Plank equations

$$\frac{\partial C_x^j}{\partial t} = \nabla \cdot D_x^j \left(\nabla C_x^j + \frac{z^j F}{RT} C_x^j \nabla \phi_x \right) \tag{2}$$

where C_x^j is the concentration of unbound ion j in space x, z^j is the charge of ion j, D_x^j is the effective diffusion of ion j in space x, F is Faraday's constant, R is the gas constant, T is the absolute temperature and ϕ_x is the potential in the space x. The conventional Nernst-Plank equations are adapted to represent the movement of ions across the cell membrane between the intra and extracellular spaces. This gives

$$\frac{\partial C_x^j}{\partial t} = \nabla \cdot D_x^j \left(\nabla C_x^j + \frac{z^j F}{RT} C_x^j \nabla \phi_x \right) + \frac{\chi J_m^j}{\alpha_x} \tag{3}$$

where J_m^j is the flux of ion j across the cell membrane. J_m^j is defined in units of mM ms^{-1} mm. The surface separating the two regions is modelled as a simple capacitor and defining the transmembrane potential to scale with intracellular charge gives

$$V_m = \frac{Q_i}{C_m} \tag{4}$$

where Q_i is the intracellular charge per unit cell membrane area and C_m is the membrane capacitance per unit cell membrane area. The charge on either side of the membrane is assumed to be equal but opposite, giving

$$Q_i = -Q_e \tag{5}$$

Separating the concentration of each ion species in the intra and extracellular space into ions that are membrane bound and make up the membrane charge (Q_x^j) and those that are in solution gives.

$$C_x^j = C_{xsol}^j + C_{xQ}^j \tag{6}$$

where C_{xsol}^j and C_{xQ}^j are the ions in solution and membrane bound ions, respectively. By assuming charge neutrality for the ions within the solute gives:

$$F \sum z^j C_{xsol}^j = 0 \tag{7}$$

Multiplying Eqn 6 by the ion species charge and Faraday's constant, then summing over all ion species in space x gives.

$$F \sum z^j C_x^j = F \sum z^j C_{xQ}^j \tag{8}$$

Converting the concentration of ions per unit volume in domain x to charge per unit cell membrane area and introducing a static charge term (η_x) that characterises all charge not attributable to C_x^j, gives

$$Q_x^j = \frac{\alpha_x}{\chi} F \sum z^j C_{xQ}^j + \eta_x \tag{9}$$

Combining with Eqn 8 gives

$$Q_x^j = \frac{\alpha_x}{\chi} F \sum z^j C_x^j + \eta_x \tag{10}$$

This defines the charge on the membrane as equal to the unbalanced charge in space x. Using the charge balance Eqn 5, gives

$$\alpha_i \sum z^j C_i^j + \alpha_e \sum z^j C_e^j + \eta_i + \eta_e = 0 \tag{11}$$

Differentiating Eqn 11 with respect to time, substituting in Eqn 3 and recognising that all transmembrane fluxes are balanced, provides

$$\alpha_i \sum z^j \nabla \cdot D_i^j \left(\nabla C_i^j + \frac{z^j F}{RT} C_i^j \nabla \phi_i \right) + \alpha_e \sum z^j \nabla \cdot D_e^j \left(\nabla C_e^j + \frac{z^j F}{RT} C_e^j \nabla \phi_e \right) = 0 \quad (12)$$

this ensures that there is no net charge accumulation in any unit volume of myocardium. Defining the relationship between the intra and extracellular potentials gives

$$V_m = \phi_i - \phi_e \quad (13)$$

Using Eqn 4 and the definition of charge (Eqn 10), then gives the algebraic definition of the transmembrane potential:

$$V_m = \frac{F}{C_m \chi} \alpha_i \left(\sum z^j C_i^j + \eta_i \right) \quad (14)$$

Rearranging Eqn 13 and substituting in the definition of V_m from Eqn 14 allows ϕ_i to be defined in terms of ϕ_e and C_x^j. Combining this definition of ϕ_i with Eqns 14, 13, 12, 3 and 2 then represents a closed set of equations. These equations are equivalent to the bidomain equations in the case of a single charge carrier and no gradient in ion concentrations, as shown below.

In cardiac myocytes many important ions, including H^+ and Ca^{2+} are heavily buffered, both within the cell and the extracellular space. To account for buffering the free and buffer bound fraction of C_x^j are calculated. In general, as $C_{xsol}^j >> C_{xQ}^j$ the effect of ions bound to the cell membrane will not be included in the buffering equations for simplicity. This gives

$$C_x^j \approx C_{xsol}^j = C_{xfree}^j + C_{xbuff}^j \quad (15)$$

where C_{xfree}^j are the unbound ions and C_{xbuff}^j are the ions bound to buffers. At this time all buffers will be treated as rapid and to a single representative buffer species, giving

$$C_x^j = C_{xfree}^j + B_x^j \frac{{C_{xfree}^j}^{n_x^j}}{{C_{xfree}^j}^{n_x^j} + K_x^{j n_x^j}} \quad (16)$$

where B_x^j, K_x^j and n_x^j are the concentration, binding affinity and Hill coefficient, respectively, for the buffer of ion j in space x. Assuming that ions bound to buffers are immobile, only C_{xfree}^j is used to calculate the diffusion and drift of ions in Eqn 3, and similarly in Eqn 12. As binding of ions to a buffer implicitly removes a charged binding site located on a static protein, Eqn 14 remains unchanged.

Due to the complex anatomy of the cardiac myocyte many sub volumes exist within the cell that affect ionic concentrations. The sum of the volume fraction (α_x) values must be less than, but do not have to be equal to, one, allowing the model to represent any volume fractions that are not directly accessible by ions. In particular the α_i variable can represent all space in the cell or can be substituted for α_{cyt} representing the volume fraction of the cytosol (a sub volume of α_i). This allows the effects of SR, mitochondrial or other subcellular structure volumes on intracellular ionic concentrations to be accounted for in the model.

Equation summary. The modelled equations are given by

$$V_m = \frac{F}{C_m \chi} \alpha_i \left(\sum z^j C_i^j + \eta_i \right) \quad (17)$$

$$\phi_i = V_m + \phi_e$$

$$C_x^j = C_{xfree}^j + B_x^j \frac{{C_{xfree}^j}^{n_x^j}}{{C_{xfree}^j}^{n_x^j} + K_x^{j n_x^j}}$$

$$\frac{\partial C_i^j}{\partial t} = \nabla \cdot D_i^j \left(\nabla C_{ifree}^j + \frac{z^j F}{RT} C_{ifree}^j \nabla \phi_i \right) - \frac{\chi J_m^j}{\alpha_i}$$

$$\frac{\partial C_e^j}{\partial t} = \nabla \cdot D_e^j \left(\nabla C_{efree}^j + \frac{z^j F}{RT} C_{efree}^j \nabla \phi_e \right) + \frac{\chi J_m^j}{\alpha_e}$$

$$0 = \alpha_i \sum z^j \nabla \cdot D_i^j \left(\nabla C_{ifree}^j + \frac{z^j F}{RT} C_{ifree}^j \nabla \phi_i \right) + \alpha_e \sum z^j \nabla \cdot D_e^j \left(\nabla C_{efree}^j + \frac{z^j F}{RT} C_{efree}^j \nabla \phi_e \right)$$

where it is important to note that for non buffered ions $B_x^j = 0$ and $C_x^j = C_{xfree}^j$.

Consistency with bidomain equations. Imposing the implicit assumptions of the bidomain equations that charge carriers are not buffered, ion concentrations are homogenous and charge is carried by a single carrier to Eqn 18, the bidomain equations can be derived. Assuming homogenous ion concentrations and considering the case of the intracellular space reduces Eqn 18 to

$$\frac{\partial C_i^j}{\partial t} = \nabla \cdot D_x^j \frac{z^j F}{RT} C_i^j \nabla \phi_i - \frac{\chi J_m^j}{\alpha_i} \quad (18)$$

Differentiating Eqn 14 for the intracellular space gives

$$\frac{\partial V_m}{\partial t} = \frac{F}{C_m \chi} \alpha_i \sum \left(z^j \frac{\partial C_i^j}{\partial t} \right) \quad (19)$$

substituting Eqn 18 into Eqn 19 gives

$$\frac{\partial V_m}{\partial t} = \frac{F}{C_m \chi} \alpha_i \sum z^j \left(\nabla \cdot D_x^j \frac{z^j F}{RT} C_i^j \nabla \phi_i - \frac{\chi J_m^j}{\alpha_i} \right) \quad (20)$$

As ion concentrations are homogenous conductivity is defined as

$$\sigma_x = \sum D_x^j \frac{z^{j2} F^2 \alpha_x C_x^j}{RT} \quad (21)$$

Then Eqn 20 reduces to

$$C_m \chi \frac{\partial V_m}{\partial t} = \nabla \cdot \sigma_i \nabla \phi_i - F \sum z^j J_m^j \quad (22)$$

Applying the single charge carrier assumption and converting from ionic flux to current gives the first bidomain equation

$$\chi \left(C_m \frac{\partial V_m}{\partial t} + I_{ion} \right) = \nabla \cdot \sigma_i \nabla \phi_i \quad (23)$$

The second bidomain equation is readily derived from applying the homogenous ion concentration assumption to Eqn 12 and multiplying by Faraday's constant (to convert from conserving ion flux to current) giving

$$\nabla \cdot \sum D_i^j \frac{z^{j2} F^2 \alpha_i C_i^j}{RT} \nabla \phi_i + \nabla \cdot \sum D_e^j \frac{z^{j2} F^2 \alpha_e C_e^j}{RT} \nabla \phi_e = 0 \quad (24)$$

Substituting in the definition of conductivity from Eqn 21 then gives the second bidomain equation

$$\nabla \cdot \sigma_i \nabla \phi_i + \nabla \cdot \sigma_e \nabla \phi_e = 0 \quad (25)$$

Modelling the Membrane Fluxes

Cardiac electrophysiology is predominantly determined by the movement of Ca^{2+}, Na^+ and K^+. For charge neutrality Cl^- must also be included in the model. To simulate the evolution of acidosis requires the inclusion of H^+, HCO_3^- and CO_2 in the model. All of these ions (and CO_2) were modelled in the intra and extracellular space, with H^+ and Ca^{2+} being buffered. The goal of the model, in this study, was not to track the propagation of the action potential but to simulate the gradients of ions that exist over the BZ. These ion gradients were modelled based on the diastolic properties of the cell. This assumption was also a requirement to enable the simulation of minutes, while remaining computationally tractable.

The membrane ion transport pathways are described first for Na^+, H^+ and HCO_3^-. Ion specific channels are then described that balance the flux of each ion species. The channel and transporter densities were determined by imposing zero net flux for each ion species, using the relative densities of Na^+ and H^+ transporters recorded experimentally, and intra and extracellular ionic concentrations and membrane potential values derived from the literature. Where possible experimental data was taken preferentially from rabbit or guinea pig data at body temperature. This limited number of constraints then allowed the model transporters and channel densities to be uniquely determined.

Sodium regulation. The model of Na^+ regulation included representations of the *NaK*, sodium calcium exchanger (*NCX*), sodium hydrogen exchanger (*NHE*), sodium bicarbonate co-transporter (*NBC*) and a lumped sodium channel (I_{Na}). *NaK* was modelled using the thermodynamically consistent equation set proposed by Smith and Crampin [19]. This model was subsequently revised by Terkildsen et al., [20] and this parameter set that was used here. The model for *NaK* was fitted to guinea pig data as limited rabbit data was available. However, the maximum flux was rescaled to match rabbit data, as described below.

The *NCX* model was taken from Weber et al., [21]. The model has been fitted to rabbit experimental data at 37°C. The *NHE* model was based on the model developed by Crampin and Smith [22] and reparameterized by Niederer and Smith [23]. In this study extracellular Na^+ and H^+ regulation of *NHE* were included. This model was fitted predominantly to sheep Purkinje data [24], although the H^+ dependence of *NHE* remains relatively consistent between species [25]. The *NBC* model was taken from Crampin and Smith [22]. The model assumes *NBC* is electro neutral, which is true for only part of the *NBC* population [25]. There was not sufficient data to fully characterise the electrogenic and electro neutral forms of *NBC*, hence the electro neutral model was used. Background Na^+ flux across residual open fast Na^+ and persistent Na^+ channels is limited when the cell is quiescent. However, some flux is still present [26] and a simple lumped background ionic flux equation was used, given by

$$J_{Na} = g_{Na}(V_m - E_{Na}) \quad (26)$$

to model the residual Na^+ flux across any open Na^+ channels. The same equation form was used for modelling all background ion channels.

Proton regulation. In the proposed model $[H^+]_i$ was regulated by *NHE*, described above, chloride-hydroxide exchanger (*CHE*), hydrolysis and buffering. Background H^+ leak or other H^+ exchangers were not considered in the general model of H^+ regulation, described here, but do include models of H^+-lactate exchange and intracellular metabolism derived H^+ sources in the model of ischemia, described below. The *CHE* model comes from Niederer et al., [27] and was fitted to guinea pig data at 37^{o}C. The hydrolysis of CO_2 into HCO_3^- and H^+ was governed by

$$J_{Hyd} = k_f [CO_2] - k_r [H^+][HCO_3^-] \quad (27)$$

where k_f and k_r are the forward and reverse rates of hydrolysis. Hydrolysis occurs in both the intra and extracellular space and the rate constants were assumed to be the same in both domains. H^+ buffering in the intra and extracellular space is due to mobile and static H^+ buffers and HCO_3^- [28]. The intra and extracellular buffering of H^+ were assumed to be instantaneous and represented by a single population of buffers. To reduce the model size, partial differential equations were only solved for the total concentration of $[H^+]_i$ or $[H^+]_e$. The concentration of free ions were then calculated by

$$[H^+]_{free} = \frac{-K_H - B_H + [H^+]_{total} + \sqrt{(K_H + B_H - [H^+]_{total})^2 - 4[H^+]_{total} K_H}}{2} \quad (28)$$

where B_H and K_H represent the concentration of the buffer and the binding affinity, respectively. This buffer model was used for both intra and extracellular H^+, with a separate set of parameters for each ion.

Calcium regulation. A simplified model of intracellular cardiac Ca^{2+} was developed assuming that Ca^{2+} in the

intracellular space reaches an approximate equilibrium over the time scales of interest. Furthermore, SERCA ATPase function was modelled with a Hill coefficient of one as opposed to two, to allow the definition of Ca^{2+} to remain deterministic. The intracellular space was assumed to consist of a sarcoplasmic reticulum (SR) and a cytosolic space. The subsarcolemmal and dyadic space are small and are also likely to be in equilibrium with the cytosolic Ca^{2+}, so were not included in the model. The Ca^{2+} dynamics were described by

$$\frac{d[Ca^{2+}]_i}{dt} = -J_{SERCA} + J_{leak} + (I_{CaL} + I_{Cab} - I_{NCX})\frac{A_m}{Fz_{Ca}} \quad (29)$$

$$\frac{d[Ca^{2+}]_{SR}}{dt} = (J_{SERCA} - J_{leak})\frac{\alpha_{SR}}{\alpha_{cyt}} \quad (30)$$

$$J_{SERCA} = V_{SERCA}\frac{[Ca^{2+}]_i^{nH}}{[Ca^{2+}]_i^{nH} + K_{SERCA}^{nH}} \quad (31)$$

$$J_{leak} = P_{leak}\left([Ca^{2+}]_{SR} - [Ca^{2+}]_i\right) \quad (32)$$

$$I_{Ca} = I_{CaL} + I_{Cab} = g_{Ca}(V_m - E_{Ca}) \quad (33)$$

where $[Ca^{2+}]_{SR}$ is the SR Ca^{2+}, J_{leak} is the flux of calcium out of the SR, J_{SERCA} is the uptake of Ca^{2+} by SERCA, V_{SERCA} is the maximum SERCA flux, P_{leak} is the diffusion permeability of the SR membrane, K_{SERCA} is the binding coefficient of Ca^{2+} to SERCA, α_{SR} and α_{cyt} are the volume fractions of the SR and cytosol, respectively, I_{CaL} is the L-type calcium channel and I_{Cab} is the background Ca^{2+} channel. In this model the background and L-type Ca^{2+} channels were modelled as a single lumped generic Ca^{2+} channel. Introducing cytosolic buffering, ignoring the effects of SR buffering and setting nH as one and assuming that the cytosol and the SR are in equilibrium then gives

$$[Ca^{2+}]_{SR} = [Ca^{2+}]_i + \frac{V_{SERCA}}{P_{leak}}\frac{[Ca^{2+}]_i}{[Ca^{2+}]_i + K_{SERCA}} \quad (34)$$

$$\begin{aligned}[Ca^{2+}]_{tot} &= [Ca^{2+}]_i + \frac{\alpha_{SR}}{\alpha_{cyt}}[Ca^{2+}]_{SR} + B_{Ca}\frac{[Ca^{2+}]_i}{[Ca^{2+}]_i + K_{Ca}} \\ &= [Ca^{2+}]_i\left(1 + \frac{\alpha_{SR}}{\alpha_{cyt}}\right) + \frac{\alpha_{SR}}{\alpha_{cyt}}\frac{V_{SERCA}}{P_{leak}}\frac{[Ca^{2+}]_i}{[Ca^{2+}]_i + K_{SERCA}} \\ &\quad + B_{Ca}\frac{[Ca^{2+}]_i}{[Ca^{2+}]_i + K_{Ca}}\end{aligned}$$

defining

$$B_{SERCA} = \frac{\alpha_{SR}}{\alpha_{cyt}}\frac{V_{SERCA}}{P_{leak}} \quad (35)$$

$$\gamma_{Ca} = 1 + \frac{\alpha_{SR}}{\alpha_{cyt}} \quad (36)$$

and collecting terms gives

$$A = \frac{\gamma_{Ca}K_{SERCA} + \gamma_{Ca}K_{buff} + B_{buff} + B_{SERCA} - [Ca^{2+}]_{tot}}{\gamma_{Ca}} \quad (37)$$

$$B = \frac{\gamma_{Ca}K_{buff}K_{SERCA} + B_{buff}K_{SERCA} + B_{SERCA}K_{buff} - [Ca^{2+}]_{tot}(K_{SERCA} + K_{buff})}{\gamma_{Ca}} \quad (38)$$

$$C = \frac{-[Ca^{2+}]_{tot}K_{buff}K_{SERCA}}{\gamma_{Ca}} \quad (39)$$

$$0 = [Ca^{2+}]_i^3 + A[Ca^{2+}]_i^2 + B[Ca^{2+}]_i + C \quad (40)$$

As C is always negative the cubic always has at least one positive real root for possible values of $[Ca^{2+}]_{tot}$. The value of $[Ca^{2+}]_{tot}$ was then found using the root finding method first proposed by Francois Viete in 1600 and reused more recently by Faber and Rudy [29]:

$$[Ca^{2+}]_i = \frac{2\sqrt{A^2 - 3B}}{3}\cos\left(\frac{\arccos\left(\frac{9AB - 2A^3 - 27C}{2(A^2 - 3B)^{1.5}}\right)}{3}\right) - \frac{A}{3} \quad (41)$$

The model of Ca^{2+} dynamics assumes that all Ca^{2+} buffers were static and that the transport of ions via mobile buffers was accounted for in the effective diffusion parameters of free Ca^{2+}. It is possible to extend the proposed model to include mobile buffers but they were assumed to play a secondary role in the current model. $[Ca^{2+}]_e$ was assumed to be buffered by a single species and was modelled using the same framework described above for H^+ (Eqn 28).

Chloride regulation. In this model Cl^- homeostasis was maintained by the CHE and the Cl^--HCO_3^- exchanger (AE), which bring Cl^- into the cell, and a Cl^- channel that allows Cl^- to flow out of the cell. The CHE model is described above. The AE model was taken from Crampin and Smith [22] and was developed using guinea pig data at 37^{o}C. The Cl^- channel uses the conventional background channel formulation. A linear H^+ dependence of the background Cl^- current was added to the model based on observations from Komukai et al., [30].

Potassium regulation. In dynamic action potential models of cardiac electrophysiology there are a large number of K^+ channels [31] that bring K^+ into the cell. This influx was balanced by the NaK pump, described above, that extrudes K^+. For the passive membrane model, all of the K^+ channels were lumped into a single background current (I_{Kb}) formulation that was set to balance the flux of K^+ on NaK. It was assumed that the

membrane potential and K^+ reversal potential are the dominant factors affecting this channel and other forms of regulation have not been considered.

Bicarbonate regulation. HCO_3^- was assumed to be regulated principally by hydrolysis and through NBC and AE. All of these components have been described above and it was assumed that there are no other HCO_3^- pathways across the membrane.

Carbon Dioxide. CO_2 is regulated primarily through hydrolysis and can diffuse relatively freely across the membrane. The model of hydrolysis is described above and CO_2 diffusion was assumed to obey Fick's law.

Model Parameters

For each transmembrane ion pathway described above, all kinetic, binding affinity and membrane potential dependencies were taken from the original models. Here the definition of geometrical parameters, ionic concentrations, buffering parameters and the density/scaling of each transmembrane pathway are motivated from data in the literature.

Geometrical parameters. The extracellular space is estimated to be between $17-30\%$ [32–35], $17.7\pm0.6\%$ and $24.6\pm0.6\%$ [33,36] of the volume of the heart in rabbit, cat, and rat hearts, respectively. This gave an α_e value of 0.2 leading to an α_i value of 0.8. The surface to volume ratio of a cell is reported as $0.31-0.35\mu$ m^{-1} [37,38] in rat and rabbit myocytes, corresponding to a χ value of $264mm^{-1}$. The relative SR volume was set to 3% of intracellular volume, giving an α_{SR} value of 0.024, based on reported values of $1.4-3.5\%$ of cell volume [37,39,40] in mouse, rat and swine. The relative mitochondrial volume (α_{mito}) was set to 0.24 based on an estimated mitochondrial cell volume fraction of 30% [37,40]. The cytosol volume fraction was set to 67% of the intracellular space, resulting in an α_{cyt} value of 0.536. To account for the effects of subscellular domains on intracellular ionic concentrations in the model, all references to α_i in Eqn 18 were replaced by α_{cyt}. A summary of geometrical parameters is given in Table 1.

Intracellular ionic concentrations. $[Na^+]_i$ has been measured using SBF1 fluorescence and Na^+ sensitive electrodes. A significant range of values have been reported from $2-10$mM [26,41–44] to $20-30$mM [34,45,46]. Early measurements of intracellular ionic concentrations were performed using ion sensitive electrodes. These experiments measure ion activity and not ionic concentration and are often performed in multi-cellular preparations, confounding measurements. For these reasons $[Na^+]_i$ in quiescent myocytes was set to 4mM, consistent with recent calibrated fluorescent measurements in isolated rabbit myocytes [26,44].

No fluorescence dye is routinely used for measuring $[K^+]_i$. Using ion sensitive electrodes Lee et al., [45] were able to calibrate their measurements of ion activity in rabbit myocytes using an estimated K^+ activity coefficient of 0.613, giving a value of 135mM. This compares with a range of $147-236$mM calculated by applying the Lee et al., K^+ ion activity coefficient to ion activity measurements in rabbit, cat and guinea pig [34,43,47,48]. Alternate measurement using flame emission spectrometry by Powell et al., [49] measured $[K^+]_i$ in rat myocytes, giving a concentration of 120.8 ± 1.7 mM. Given the lower values of the two calibrated measurements, $[K^+]_i$ was set to 135 mM.

No dye is routinely used for measuring Cl^- concentration in cardiac cells, however, $[Cl^-]_i$ can be measured using ion sensitive electrodes. Cl^- activity has been reported as $14-20$ mM [35,48,50,51] in sheep, rabbit and guinea pig heart cells. Estimations of $[Cl^-]_i$ from total tissue Cl^- concentrations have resulted in values of 38.9 ± 2.5 mM [35] and 16.2 mM [34] in rabbit cells and $19.4\pm1.2\mu$ mol/g dry wt (or 9.7 mM using the 0.49 mM per μmol/g dry wt scaling factor from Bers [52]) in rat. The higher value of 39 mM may be attributed to the higher extracellular space used in these calculations (30% as compared to 20%). Considering the relative convergence of values $[Cl^-]_i$ was set to 18 mM.

Resting free Ca^{2+} is measured using calibrated fluorescence measurements. These measurements range from $44-100$ nM in rabbit and guinea pig preparations [53–57]. Given this consistency the $[Ca^{2+}]_i$ will be set to 80 nM. SR Ca^{2+} concentration is calculated from integrating the current across the cell membrane following the release of Ca^{2+} from the SR in response to caffeine. These measurements show two populations with high values in rat ($73-140$ μM [58–61]), canine (80 μM [62]), rabbit (87–106 μM [60,61]) and ferret (76 μM [63]), compared to lower measurements in guinea pig ($17.9-27$ μM [58,64]). Given that the majority of species have a higher reported concentration, including rabbit, simulations were run with SR Ca^{2+} load set to 100 μM. The buffering of Ca^{2+} can be described by Hill equation(s), mass action equation(s) or a constant buffering power. To compromise between biophysics and complexity, buffering was modelled by a single Hill equation. Hove-Madsen and Bers [65] fitted Ca^{2+} buffering in rabbit myocytes using two Hill curves; however, the lower affinity buffer will not play a significant role at passive diastolic Ca^{2+} concentrations. For this reason the high affinity site, with cooperativity reduced from 1.27 to unity, was used to model Ca^{2+} buffering, giving a buffer concentration of 208.98 μM (converted using a scaling factor of 2.43 from Bers [52]) and an affinity of 0.42 μM. This model of Ca^{2+} buffering in rabbit is similar to the concentration/affinity values of $162/0.63$ μM [66], $121/0.65$ μM [67] and $128-162/0.45-0.53$ μM [68] values measured in other species.

pH_i has been measured using H^+ sensitive electrodes and fluorescence dyes. Measurement of pH_i consistently falls within the range of $7.0-7.25$ [57,69–71] in either HEPES or HCO_3^- buffered solutions. In the model pH_i was set to 7.1. H^+ are heavily buffered in the cytosol by intrinsic buffers and HCO_3^-. Here the buffering of H^+ by HCO_3^- was modelled explicitly and the intrinsic buffers were assumed to be in rapid equilibrium. Leem et al., [70] measured (and modelled) H^+ buffering by two populations of buffers with binding affinity pK values of 6.03 and 7.57 and concentrations of 84.22mM and 29.38mM. Zanbioni et al., [25] differentiated between mobile and fixed buffers and found that the fixed buffers had a consistent concentration of $50-70$mM and binding affinity (pK) value of $6.1-6.2$ across rat, rabbit and guinea pig, while the mobile buffers had a constant β value of $approx10$. Fitting a single buffering curve to these two

Table 1. Geometric variables.

Variable	Value
α_i	0.8
α_e	0.2
χ	264 mm^{-1}
α_{cyt}	0.536
α_{mito}	0.24
α_{SR}	0.024

doi:10.1371/journal.pone.0060323.t001

Table 2. Intra and extracellular free ion concentrations.

Ion	Concentration (mM)	
	Intracellular	Extracellular
Na^+	4.0	140
K^+	135	4.0
Cl^-	18	110
Ca^{2+}	80×10^{-6}	1.2
H^+	$10^{-4.1}$	$10^{-4.4}$
CO_2	1.17	1.17

doi:10.1371/journal.pone.0060323.t002

models over a pH range of $6.5-7.5$ gives concentrations of $64-68$mM and pK values of $6.45-6.65$, which gave a value of 65mM and pK value of 6.5 for this model.

Extracellular ionic concentrations. The concentration of the majority of ions in the extracellular space have been measured in canine [46,72], rat [36,73] and cat [74] hearts. These measurements provide a consistent range of ion concentrations for Na^+, K^+ and Cl^-, giving $[Na^+]_e$ as $134-159$mM, $[K^+]_e$ as $3.3-5.8$mM and $[Cl^-]_e$ as $105-120$mM. In the model $[Na^+]_e$ was set to 140mM, $[K^+]_e$ was set to 4mM, consistent with measurements in guinea pig hearts [75] and rabbit atrium [76] and $[Cl^-]_e$ was set to 110mM. The $[Ca^{2+}]_e$ values reported range from $1.03-5.16$mM, however, these values do not differentiate between buffered and ionized Ca^{2+}. The properties of Ca^{2+} buffering in the extracellular space are not well characterised and are generally ignored in previous cardiac cell models. To approximate the buffering properties of extracellular Ca^{2+} using a simple single species steady state mass action model, with no cooperative binding, requires two parameters, the concentration of the buffer and the binding affinity. Assuming the ratio of free Ca^{2+} in the extracellular space to bound ions is similar to serum [77] and assuming that the primary buffer of Ca^{2+} in the extracellular space are phospholipids, then extracellular Ca^{2+} buffering will have a binding affinity of 1.1mM [78], within the range observed across multiple species [79], and a buffer concentration of 2.3mM based on a free Ca^{2+} concentration of 1.2mM and assuming 50% of Ca^{2+} are bound to buffers [77]. pH_e was set to 7.4, to be consistent with the majority of experimental studies [57,69–71] and measurements across a range of species [80]. Limited measurements were available to model $[H^+]_e$ buffering, however, Yan and Kleber [81] reported 39 mM of buffered H^+ in the extracellular space. By assuming similar binding affinities for the intra and extracellular buffers and that pH_e is 7.4, then gave a concentration of extracellular proton buffers of 350mM. A summary of ion concentrations and buffering parameters are given in Table 2 and Table 3, respectively.

The concentration of CO_2 was calculated using the parameters proposed and measured for guinea pig ventricular myocytes at 37^oC by Leem and Vaughan-Jones [82]. The concentration of CO_2 in the extracellular solution was calculated using

Table 3. Buffering Parameters.

Parameter	Value (mM)	
	Intracellular	Extracellular
B_H	65	350
K_H	$10^{-3.5}$	$10^{-3.5}$
B_{Ca}	0.209	2.3
K_{Ca}	0.42×10^{-3}	1.1

doi:10.1371/journal.pone.0060323.t003

$$[CO_2]_e = \alpha_{CO_2}(\%CO_2)P_{atm} \tag{42}$$

where α_{CO_2} is the solubility of CO_2, set to 0.0307 mM $mmHg^{-1}$ from human measurements at pH 7.4 and 37^oC [83], $\%CO_2$ is the fraction of air that is CO_2, set to 5% at baseline and P_{atm} is atmospheric pressure, set to 760 $mmHg^{-1}$. This gives a partial pressure of CO_2 (P_{CO_2}) of 38 mmHg, consistent with although slightly higher than the 34 ± 3 mmHg measured in rabbit hearts [84]. The hydration of CO_2 was modelled by a mass action reaction (Eqn 27). The k_f and k_r values were measured and modelled by Leem and Vaughan-Jones in guinea pig myocytes at 37^oC [82], giving values of $0.365s^{-1}$ and $3.11\times10^5s^{-1}$, respectively, resulting in an equilibrium constant of $10^{-6.2}$. The rate of hydration of CO_2 was assumed to be similar in both the intra and extracellular space. The movement of CO_2 across the cell membrane was modelled by Fick's law. Previous models have used permittivity values of $0.058mms^{-1}$[82], based on measurements in red blood cells. This value was reused despite its lack of species and cell type consistency, as there were no recent studies characterising the permeability in cardiac myocytes and the high permeability leads CO_2 to be close to equilibrium between the intra and extracellular spaces.

Current, exchanger and pump densities. The model of each transmembrane ion pathway (y) was separated into a kinetic regulatory component (γ_y) dependent on transmembrane potential and ionic concentrations, and a scalar (V_y) representing either the maximum flux or channel conduction of the pathway. The flux across a pathway (G_y) is then given by

$$G_y = \gamma_y V_y \tag{43}$$

The V_y values were determind by calculating all of the γ_y values (excluding γ_{NBC}, γ_{hyd} and γ_{CO2} as $[CO_2]_i$ and $[HCO_3^-]_i$ were unknown) using the ionic concentrations in Table 2 and assuming a membrane potential of -80 mV. The remaining unknown V_y and ionic concentrations were then determined from a limited number of measurements and by enforcing a zero net flux condition described by

$$\begin{bmatrix} \gamma_{Nab} & -3\gamma_{NaK} & 3\gamma_{NCX} & \gamma_{NHE} & \gamma_{NBC} & & & & & & \\ & 2\gamma_{NaK} & & & & \gamma_{Kb} & & & & & \\ & & \gamma_{NCX} & & & & \gamma_{Cab} & & & & \\ & & & -\gamma_{NHE} & & & & \gamma_{CHE} & \gamma_{hyd} & & \\ & & & & -\gamma_{NBC} & & & & \gamma_{hyd} & -\gamma_{AE} & \\ & & & & & & & \gamma_{CHE} & & \gamma_{AE} & \gamma_{Clb} \\ & & & & & & & & -\gamma_{hyd} & & \\ & & & & & & & & & & \gamma_{CO2} \end{bmatrix} \begin{bmatrix} V_{Na} \\ V_{NaK} \\ V_{NCX} \\ V_{NHE} \\ V_{NBC} \\ V_{kb} \\ V_{Cab} \\ V_{CHE} \\ V_{hyd} \\ V_{AE} \\ V_{Cl} \\ V_{CO_2} \end{bmatrix} = 0 \quad (44)$$

As the parameters for hydrolysis and permeability of the cell membrane to CO_2 (P_{CO_2}, k_f and k_r) were derived from the literature, the constraints on V_{CO_2} and V_{hyd} were used to determine the concentrations of $[CO_2]_i$ and $[HCO_3^-]_i$, respectively. Measurements of transmembrane Na^+ influx gave G_{Na} as 0.25×10^{-5} mM ms^{-1}, G_{NCX} as 0.48×10^{-5} mM ms^{-1}, G_{NHE} as 0.20×10^{-5} mM ms^{-1} and G_{NBC} as 0.20×10^{-5} mM ms^{-1}

Table 4. Qualitative changes in intracellular ionic concentrations or membrane potential in response to changes in extracellular ionic concentration or inhibition of membrane transporters.

Protocol		Change in Concentration or Potential						Reference
Variable	**Change**	$[K^+]_i$	$[Ca^{2+}]_i$	$[H^+]_i$	$[Cl^-]_i$	$[Na^+]_i$	V_m	
1-24-9 $[Na^+]_e$								
	Decrease		↑	↑	↑	↓	↓x2 ↑x4	[160–163]
								[164–166]
	Increase			↓ ↔		↑	↓	[167,168]
$[Ca^{2+}]_e$								
	Decrease	↓	↓	↓		↑	↔ ↑	[163,169,170]
	Increase		↑			↓	↑	[171,172]
$[K^+]_e$								
	Decrease	↓ ↔	↔	↔	↔	↑	↓	[160,161,173,174]
								[71,162,175,176]
	Increase	↑ ↔	↑ ↔	↔	↑ ↔	↓	↑	[50,161,175,177,178]
								[131,173,176,179,180]
HCO_3^-/CO_2								
	Increase		↑	↑	↓		↑	[71,166,181–183]
$[Cl^-]_e$								
	Decrease	↑		↓	↓	↓	↑	[184–186]
								[50,71,187]
	Increase			↑	↑	↑	↓	[50,184,187]
$[H^+]_e$								
	Increase		↑	↑		↓ ↔ ↑	↔	[161,165,166,188]
NaK								
	Inhibition	↓	↑	↑	↑	↑	↔ ↑	[43,170,175]
								[35,160,177,189]
NHE								
	Inhibition		↓	↑		↓	↑	[44,166]

doi:10.1371/journal.pone.0060323.t004

[85]. The G_{NaK} Na^+ flux was assumed to be equal to the sum of all Na^+ influx. As the model does not include Na^+-K^+-2-Cl^- co-transporter (NaK2Cl) or Na^+-Mg^{2+} exchanger (NaMg), primarily due to the limited data to constrain the kinetics, G_{NaK} was reduced from the flux measured by Despa et al., [85] to 1.13×10^{-5} mM ms^{-1}. Setting these G_y values defines V_{Na}, V_{NCX}, V_{NHE}, V_{NaK}, V_{kb} and V_{Cab}. In the experimental and modelling work by the Vaughan-Jones group [70,86] the relative size of G_{CHE} to G_{NHE} is $0.12-0.19$ at $pH_i=7.1$, this gave an estimated ratio of 0.16. Scaling G_{NHE} determined from [85] by 0.16 provided an estimate of G_{CHE} of 0.032×10^{-5} mM ms^{-1}. This allows V_{CHE} and G_{hyd} to be defined. G_{hyd} must be balanced by G_{CO2} and as P_{CO_2} and $[CO_2]_e$ were known, this flux was used to set $[CO_2]_i$. Combining the pH_i and $[CO_2]_i$ concentrations with the defined hydrolysis parameters and the known value of G_{hyd} then gave $[HCO_3^-]_i$. Knowing G_{hyd} and G_{NBC} gave G_{AE} and hence V_{AE}. Similarly, G_{Cl} was calculated from G_{AE} and G_{CHE},which gave V_{Cl}. Finally, V_{NBC} was calculated using G_{NBC} and γ_{NBC}, calculated using the derived $[HCO_3^-]_i$ value. By automating this parameter derivation process the model parameters could be updated to ensure static ion concentrations, and hence membrane potential, for any perturbation in model parameters or ionic concentrations. Parameters for all simulations in this study were derived following this process.

Intracellular calcium dynamics. The intracellular regulation of Ca^{2+} was treated as an equilibrium system. This resulted in the SR effectively acting as an additional buffer on $[Ca^{2+}]_i$. The parameters V_{leak}, V_{SERCA}, K_{SERCA}, α_{SR} and α_{cyt} were defined from enforcing a zero net flux constraint and experimental measurements. Measurements of K_{SERCA} are similar in rat and

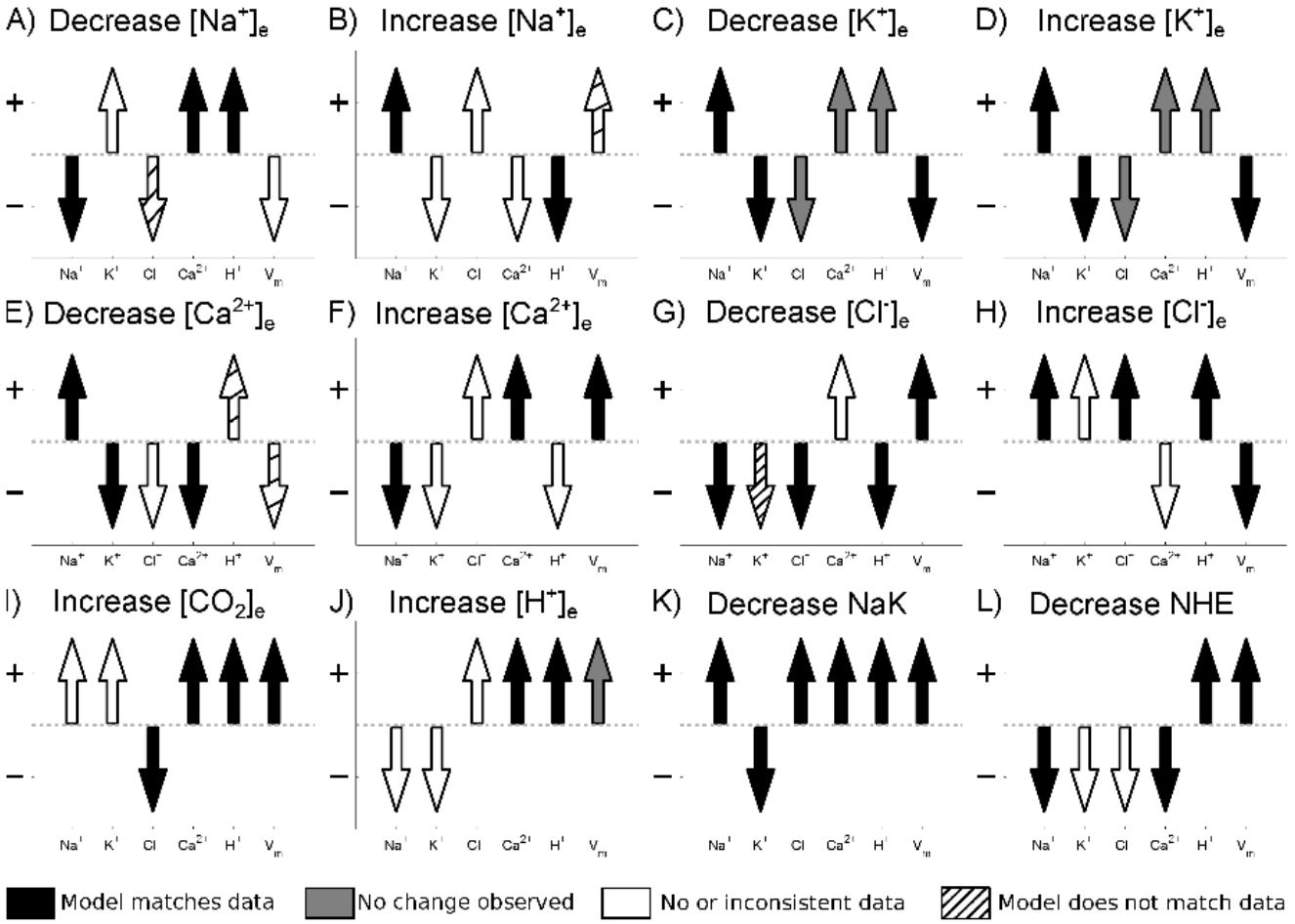

Figure 1. Cell membrane model validation. Arrow direction shows model prediction for the change in intracellular concentrations and membrane potential for a change in extracellular ion concentrations or inhibition of membrane transporter as indicated by the panel label. The color of the arrow indicates how the model compares with experimental data, summarised in Table 4. Black arrows indicate where the model matches experimental data, white arrows indicate where there is no or inconsistent data, gray arrows indicate where no change was observed experimentally and striped arrows indicate where the model does not match experimental data. Data was considered inconsistent if different studies reported opposite changes in intracellular ion concentration or membrane potential in response to a change in extracellular ionic concentrations (for example the change in membrane potential following a decrease in $[Na^+]_e$). In cases where one study reported no change in intracellular ion concentration or membrane potential and another found a change, it was assumed that the change was correct (for example the change in $[K^+]_i$ in response to an increase or a decrease in $[K^+]_e$). For example in panel A) corresponding to a decrease in $[Na^+]_e$ (as indicated by the panel label), the experimental data comes from row 1 of Tableô 4. The model predicts that $[Na^+]_i$ decreases and that $[Ca^{2+}]_i$ and $[H^+]_i$ increase, consistent with experimental measurements and the arrows are shaded black. There is no consistent observed change in the transmembrane potential so the V_m arrow remains white. No data is available for the change in $[K^+]_i$ in response to a decrease in $[Na^+]_e$ so the K^+ arrow remains white. The model predicts a decrease in $[Cl^-]_i$ yet experimental measurements found an increase, hence the Cl^- arrow is striped.
doi:10.1371/journal.pone.0060323.g001

rabbit [65] and have been reported as 0.260–0.350μM in rabbit [65,87] and 250–280μM in rat [65,87,88]. A value of 0.3μM was used in the model. J_{Leak} is reported as 0.001–0.012 μMms^{-1} in rabbit, mouse and rat [54,89–91]. A value of 0.01μMms^{-1} was used in the model. Enforcing a zero net flux constraint on the SR gave J_{SERCA} as 0.038 μMms^{-1}, comparable with values of 0.03–0.08μMms^{-1} measured in rabbit [65,87,92] with units converted using scale factors from Bers [52].

Membrane Model Validation

To validate the passive membrane model, a series of tests based on the response of the cell models intracellular ionic concentrations and transmembrane potential to changes in extracellular ionic concentrations or inhibition of major ion transporters was performed. In order to maximise the number of tests the model was compared against data from cardiac cells, regardless of temperature, species or preparation type. This maximised the number of tests but meant that a quantitative comparison was not valid and so only a qualitative comparison was performed. A summary of experimental data used in the validation is provided in Table 4. Fig. 1 shows the comparison between the model and data. From the 72 simulations performed 43 matched the experimental data, data was not available or was inconsistent for 19, changes were too small to be measured in 5 and the model did not match experiments in 5 cases.

Diffusion Parameters

The tissue model required the definition of diffusion parameters for each of the ionic species in the intra and extracellular space. The diffusion parameters used in the model were all for the apparent diffusivity of free ions, lumping the effects of any mobile buffers, tortuosity and gap junctions into a single diffusion parameter. Using Eqn 21 the conductivity parameters were shown to be directly related to the conductivity parameters in the bidomain equations. From the review of bidomain conductivities and relative values in the intra and extracellular space by Roth [93] a conductivity value of 0.25 Sm^{-1} was taken for both the intra and extracellular space. This conductivity, along with the ionic concentrations from Table 2, were used to derive the diffusion parameters. The apparent diffusion of H^+ and HCO_3^- are 1.52×10^{-7}mm^{2}ms^{-1} and 7.7×10^{-7}mm^{2}ms^{-1} in the >intracellular space [86] and were assumed to be similar in the extracellular space. The apparent diffusion constant of Ca^{2+} (including the effects of mobile buffers) has been estimated from experimental measurements in previous modelling studies as $0.4-3\times10^{-7}$mm^{2}ms^{-1} [94–96]. Here a value of 1.5×10^{-7}mm^{2}ms^{-1} [94] was used and the effect of diffusion in the SR was not included, as it was assumed to be non contiguous between cells. It was assumed that Ca^{2+} diffusion is limited by buffering, resulting in the same value in the intra and extracellular space. Na^+, K^+ and Cl^- were all assumed to have a common diffusion coefficient in either the intra or extracellular space as these ions are only nominally buffered and are only affected by gap junctions and tortuosity. Diffusion of CO_2 was estimated from previous modelling/experimental studies of CO_2 in tissue as 11.3×10^{-7}mm^{2}ms^{-1} [97], and was assumed to be the same in the intra and extracellular space. Solving Eqn 21 for the diffusion of intra and extracellular Na^+, K^+ and Cl^- gives the diffusion parameters summarised in Table 5.

Table 5. Effective ion diffusion parameters.

Ion	Diffusion Constant (10^{-7}mm^{2}ms^{-1})	
	Intracellular	Extracellular
Na^+	7.7	12.9
K^+	7.7	12.9
Cl^-	7.7	12.9
Ca^{2+}	1.5	1.5
H^+	1.52	1.52
HCO_3^-	7.7	7.70
CO_2	11.3	11.3

doi:10.1371/journal.pone.0060323.t005

Finally, the effects of $[H^+]_i$ on gap junction conductivity were included. Measurements in cell pairs by Swietach et al., [98] have demonstrated that the permeability of gap junctions has a biphasic dependence on the $[H^+]_i$ concentration. To introduce these effects into the model the intracellular diffusion constants were scaled by

$$\gamma_{diff}=\frac{[H^+]_i^{n1}}{[H^+]_i^{n1}+K_{d1}^{n1}}\frac{K_{d2}^{n2}}{K_{d2}^{n2}+[H^+]_i^{n2}} \tag{45}$$

where $n1/K_{d1}$ and $n2/K_{d2}$ are the cooperativity and binding affinity for the activation and deactivation of gap junctions by protons, respectively and γ_{diff} scales all intracellular diffusion constants. Using the measured parameters from end-to-end cell pairs in Swietach et al., [98] $n1=2.062$, $n2=1.81$, $K_{d1}=10^{-3.959}$mM and $K_{d2}=10^{-3.934}$mM. In this model of proton effects on gap junction permeability there is an implicit assumption that the gap junction permeability plays a dominant role in defining diffusion. At this stage no other regulators of permeability were included in the model, notably Ca^{2+} regulation is absent but this can readily be included in the modelling framework as required.

Simulating Ischemia

In this study the effect of NaK inhibition, I_{Kb} activation and respiratory and metabolic acidosis during ischemia on cell ionic homeostasis were considered. This list is not exhaustive and absent factors are discussed below. Ischemia was modelled by respiratory acidosis, metabolic acidosis, increased K^+ channel conductance and decreased NaK function. The specific time course of each of these changes is poorly characterised. Previous modelling studies have assumed that changes in cell function with ischemia have evolved linearly [99] or as a nonlinear function of prescribed metabolite concentrations [20]. To avoid any undue bias from the arbitrary selection of a time course, all changes are initially considered instantaneous.

NaK inhibition and K^+ channel activation were modelled by scaling the respective fluxes. Respiratory acidosis was assumed to result from an imbalance of production and washout of CO_2. To simulate this, an (implicitly electro neutral) intracellular source of CO_2 was introduced into the ischemic region. There was no flux of CO_2 out of the extracellular space and this resulted in a build up of CO_2 in both the intra and extracellular space in the ischemic region.

To model metabolic acidosis required the introduction of an additional intracellular H^+ source. However, introducing a source of cations into the cell compromised the conservation of charge constraint. To provide an electro neutral source of H^+ required

the concurrent introduction of a source of anions that match the production of H^+ inside the cell. It was implicitly assumed that the anions entered the cell in an electro neutral form with an H^+ bound, and the anions and H^+ separate within the cell due to metabolic processes. The source of H^+ in ischemia is likely to be due to increased ATP production through glycolysis [100]; in the absence of oxygen this also results in increased lactate production. As lactate readily dissociates from H^+ it was assumed that the anion source that matches H^+ flux has similar characteristics to lactate including transmembrane regulation via the lactate-H^+ membrane exchanger MCT1 [101]. Given the ambiguity in structure, MCT1 was modelled as an ordered exchanger, using the kinetic parameters from Vinnakota and Beard [102] and the maximum influx value of 4.8×10^{-5}mMms^{-1} recorded in guinea pig myocytes [103]. In the absence of metabolic acidosis, lactate concentration was assumed to be nominal, consistent with the small flux of lactate observed in rabbit hearts under normal conditions [104]. Model simulations were performed on a 1D strand with length 32 mm, oriented in the preferred conduction or fibre direction, with a transition between ischemic and viable tissue at 16 mm to ensure the simulation captured the BZ width with nominal boundary condition artefacts. The transition between viable tissue and ischemic tissue was approximated by a Hill equation with a Hill coefficient set to ensure a steep transition between the ischemic region and viable tissue over 440μm, consistent with the rapid drop in oxygen pressure across the BZ in swine [105].

Numerical Methods for Tissue Model

The nonlinear equations were solved using a fully implicit finite difference scheme with a line search Newton-Raphson method. The transmembrane flux component of the Jacobian was

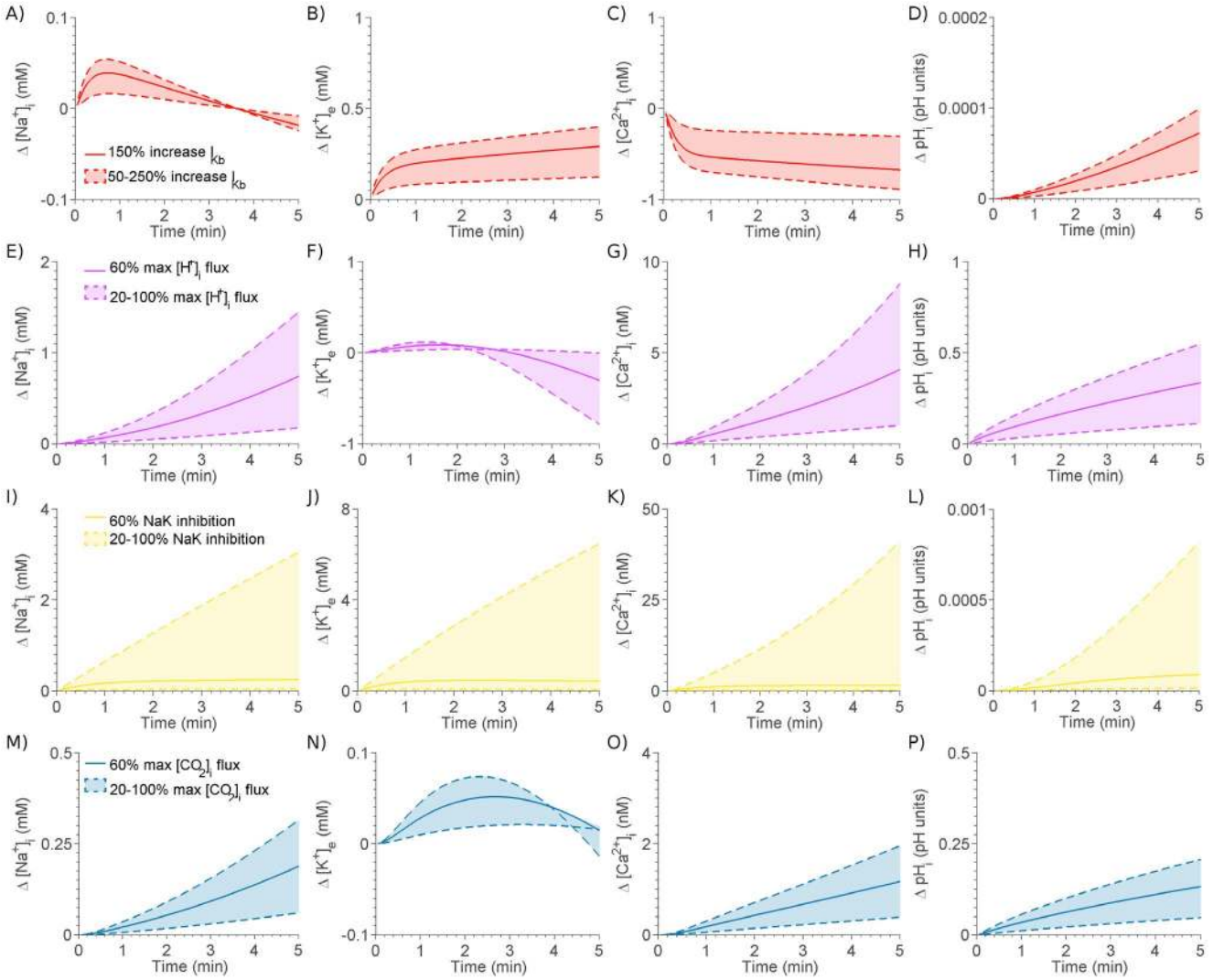

Figure 2. Effect of individual components of ischemia on the change in $[Na^+]_i$ (column 1), $[K^+]_e$ (column 2), $[Ca^{2+}]_i$ (column 3) and pH_i (column 4). Effect of 50–250% increase in I_{Kb} (red shaded region enclosed by dashed line) and a 150% increase in I_{Kb} (red line) on A) $[Na^+]_i$, B) $[K^+]_e$, C) $[Ca^{2+}]_i$ and D) pH_i. Effect of 20–100% maximum $[H^+]_i$ flux (purple shaded region enclosed by dashed line) and 60% maximum $[H^+]_i$ flux (purple line) on E) $[Na^+]_i$, F) $[K^+]_e$, G) $[Ca^{2+}]_i$ and H) pH_i. Effect of 20–100% NaK inhibition (yellow shaded region enclosed by dashed line) and a 60% NaK inhibition (yellow line) on I) $[Na^+]_i$, J) $[K^+]_e$, K) $[Ca^{2+}]_i$ and L) pH_i. Effect of 20–100% maximum $[CO_2]_i$ flux (blue shaded region enclosed by dashed line) and a 60% maximum $[CO_2]_i$ flux (blue line) on M) $[Na^+]_i$, N) $[K^+]_e$, O) $[Ca^{2+}]_i$ and P) pH_i.
doi:10.1371/journal.pone.0060323.g002

calculated using finite differencing with the remainder calculated analytically. The Jacobian was inverted directly using MatLab and was only recalculated if the residual fails to decrease or convergence was not reached within 10 Newton-Raphson iterations.

The dependence of the BZ width on the spatial and temporal discretizations was determined to test for numerical convergence. The width of the transition for each ion concentration between the viable and ischemic region, referred to as the BZ width for each ion, was calculated by fitting a Hill curve to each ionic profile. The width of the BZ for each ion was then calculated as the distance between 10 and 90% of the change in concentration.

A convergence analysis was performed and a mesh discretization of 50μm and a time step of 1000ms was used. Increasing the spatial discretization by a factor of 2 results in a maximum change in BZ width of any ion of 0.001mm. Decreasing the time step to 100ms increases the maximum BZ width of any ion by 0.001mm.

Results

The individual effects of each of the four components of ischemia were first demonstrated. A combined model of ischemia was then developed and the width and magnitude of the changes in ionic concentrations across the ischemic BZ were predicted. The effect of movement of K^+, Na^+ and Cl^- within and between intra and extracellular spaces across the BZ were calculated to show the net movement of ions across the BZ.

Simulating Individual Components of Ischemia

The level of inhibition of NaK, the activation of I_{Kb} and the level of CO_2 and H^+ production in the cell during ischemia is not known. To investigate the effects of each of these aspects of ischemia, they were each individually introduced into the model at five levels of severity, for $x>16$mm along a 32mm strand. Fig. 2 shows the effect of each component on the change in $[Na^+]_i$, $[K^+]_e$, $[Ca^{2+}]_i$ and pH_i across the ischemic BZ. The range of alterations in ion concentrations is shown by the shaded regions. The minimum and maximum changes in each component are shown by dashed lines and the mid change is shown by the solid line. NaK (yellow) was inhibited by up to 100% (no flux) in 20% increments, I_{Kb} (red) was scaled by up to 250% in 50% increments, metabolic acidosis was simulated by introducing an H^+ flux in five increments up to a maximum value of $0.1\mu\text{Mms}^{-1}$ and respiratory acidosis (blue) was simulated by a intracellular CO_2 flux increased in five increments up to a maximum value of $0.12\mu\text{Mms}^{-1}$.

Modelling Ischemia

Inherently, there is no single mode of ischemia and the relative contribution of acidosis, NaK inhibition or I_{Kb} activation will depend on the residual flow, age, gender, disease state, location of ischemic region and species under study. To provide a representative case to study, 5 minutes of ischemia were simulated in the presence of all four ischemic mechanisms that match representative results from the literature.

Partial pressure measurements of CO_2 in canine ischemic models show a $100-300\%$ increase in CO_2 partial pressure following occlusion, depending on the level of flow inhibition, after $10-15$ minutes. The elevation in CO_2 was approximately linear over time and hence in the model it was assumed CO_2 concentration increases by 150% increase in the first 5 minutes of ischemia [106,107]. This corresponded to an increase in the concentration of CO_2 in the model from 1.1mM to 2.8mM. In the model respiratory acidosis was caused by an increase in $[CO_2]_i$ flux that cannot be vented from the extracellular space. Although it is recognised that the decrease in pH_e due to metabolic acidosis will also contribute to elevated $[CO_2]_e$, initially the CO_2 flux was set at a 60% level to achieve an increase in CO_2 concentration to 2.2mM, which resulted in a decrease of pH_i to 7.0. During ischemia pH_i decreases rapidly before plateauing after approximately 15 minutes. The decrease in the initial 5 minutes has been reported to fall between 0.2 to 0.5 pH units in rat [108], ferret, [109] and guinea pig [110] preparations. Respiratory and metabolic acidosis will both contribute to this drop in pH_i. In the model setting the level of intracellular H^+ flux to 30% caused a 0.17 pH unit drop and an increase in $[CO_2]_e$ to 1.6mM. Combined metabolic and respiratory acidosis caused a 0.28 unit drop in pH and an increase in $[CO_2]_e$ to 2.85mM.

In studies of ischemia $[Na^+]_i$ tends to increase linearly with time. In the rat heart ischemia caused an increase in $[Na^+]_i$ by $78\pm8\%$ over 21 minutes [111], by 200% after 40 minutes [112], from 10.5mM to 25mM during 30 minutes ischemia [113], by 170%, 248%, 391% and 405% after 9, 15, 21 and 27 minutes, respectively [114], by two fold over 20 minutes [115], from 6.9mM to 10mM over 30 minutes [116], by $108-120\%$ over 30 minutes [117], by 408% over 27 minutes [118], no change over 10 minutes [108] and by $104-130\%$ over 30 minutes [119]. Changes in $[Na^+]_i$ in guinea pig hearts during ischemia is controversial with reports of a decrease from 8.8mM to $4.7-7.6$mM over $10-15$minutes [120] and of an increase of 108% over 15 minutes [121]. Only considering the cases where $[Na^+]_i$ increases, as these represent a repeatable consensus result, the range of expected increases in $[Na^+]_i$ over a 5 minute period is $7.5-94\%$, assuming a linear increase with time. These cluster into two groups with ranges $7.5-38\%$ and $75-94\%$. In the model reducing the maximum flux of NaK by 86% caused an increase in $[Na^+]_i$ to 4.95mM (24%) in the absence of acidosis or 5.57mM (39%) in the presence of the acidotic components of ischemia, described above.

Given the inhibition of NaK and levels of respiratory and metabolic acidosis a sweep of I_{Kb} activation values was performed in the presence of these changes to achieve the desired level of extracellular K^+ accumulation. During ischemia, $[K^+]_e$ increases over three characteristic phases, with the first phase occurring during the initial 5 minutes of ischemia prior to reaching a plateau from minutes 5 to 10, before increasing again. In guinea pigs, ischemia caused $[K^+]_e$ to increase from 4.2 to 12.6mM over 10 minutes [122] or 4 to 5.8mM over 6 minutes [123]. In swine, ischemia caused $[K^+]_e$ to increase from $3.3-4.2$mM to $10.1-11.5$mM after $7-8$ minutes [124,125]. In rat, ischemia caused an increase from 4.2mM to 8mM over 5 minutes [110], although other groups have seen a biphasic change in $[K^+]_e$ in rat with an increase from 5mM to 8.3mM before falling back to 6mM then continuing to rise again, observed over the first 8.2 minutes [126]. In rabbit, ischemia caused $[K^+]_e$ to increase from $4-4.5$mM to $6-9.4$mM over $5-10$ minutes [10,110,125]. In canine, $[K^+]_e$ increases from $3.2-4.2$mM to $8.1-14.5$mM after $6-12$ minutes [127,128]. These results indicate an increase in $[K^+]_e$ from 4mM to $10-14$mM after 10 minutes and assuming 80% of this rise occurs in the first 5 minutes [127], and combined with the 5 minute data gives an estimate of $[K^+]_e$ after 5 minutes of ischemia as $5.5-11$mM. In the model an increase in I_{Kb} of 120% was used to achieve an elevation of $[K^+]_e$ to 6.5mM, resulting in an increase in the membrane potential of 6.6mV to -73.4mV. This is consistent with measurements in cat ($5.4-8.1$mV over 10 minutes) [129,130], sheep (5mV over 5 minutes) [131], guinea pigs (13.12mV over 20 minutes) [132] and

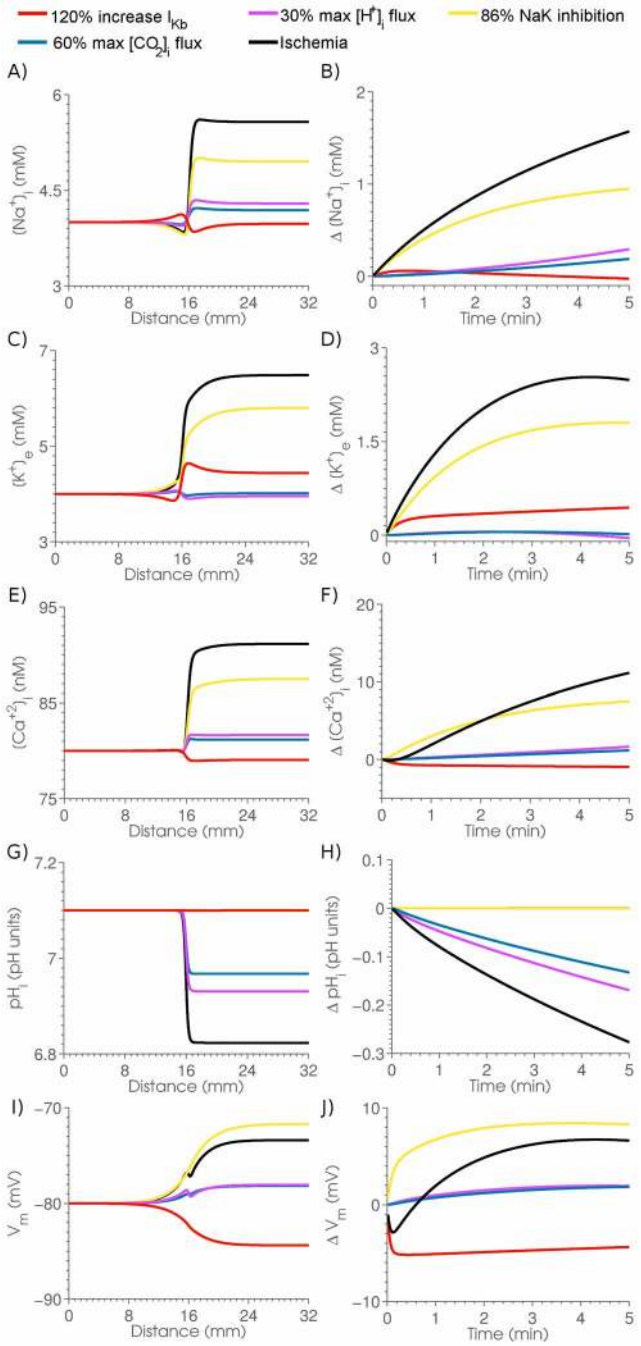

Figure 3. Evolution and profile of A-B) $[Na^+]_i$, C-D) $[K^+]_e$, E-F) $[Ca^{2+}]_i$, G-H) pH_i and I-J) membrane potential across the BZ due to each component of ischemia. Complete ischemia, *NaK* inhibition, I_{Kb} inhibition, respiratory acidosis and metabolic acidosis are represented by black, yellow, red, blue and purple lines, respectively. Column 1 shows the profile of ionic concentrations and membrane potential after 5 minutes and column 2 shows the evolution of the change in magnitude in ionic concentrations and potential across the border zone with time.
doi:10.1371/journal.pone.0060323.g003

mice (16mV over 10 minutes) [133], but less than measurements in rabbit (33mV over 12 minutes [10]) and guinea pig (32.5mV over 15 minutes [120] or 22–29mV over 30 minutes [134–136]). The broad variation in membrane potential changes was not

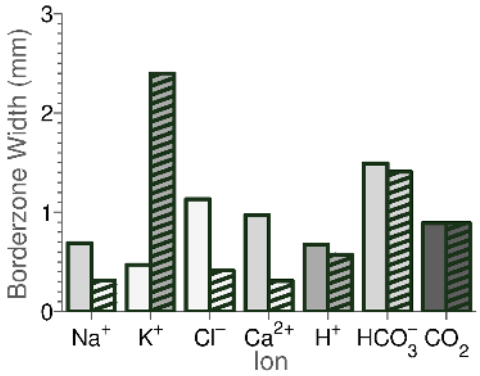

Figure 4. Width of ionic BZ. Gray scale represents magnitude of gradient with white indicating no gradient. Solid bars indicate intracellular gradient and striped bars indicate extracellular gradient.
doi:10.1371/journal.pone.0060323.g004

unexpected given the range of changes in $[Na^+]_i$ and $[K^+]_e$ reported and in simulations an intermediate value has been achieved.

The individual and combined effects of the four components of ischemia on the temporal evolution of the maximum change in ionic concentrations and the spatial concentration and potential distribution profile after 5 minutes of simulated ischemia are shown in Fig. 3. As ischemia progressed, $[Na^+]_i$ continued to increase. The early rise was attributed to *NaK* inhibition; the later increases were due to metabolic and respiratory acidosis. The early rise in $[K^+]_e$ was significantly affected by *NaK* inhibition with I_{Kb} activation playing a greater role as ischemia progresses and the membrane potential diverges from the K^+ reversal potential. The decrease in pH_i was solely due to acidosis with no impact from I_{Kb} activation or *NaK* inhibition. $[Ca^{2+}]_i$ elevation was contributed to principally by *NaK* inhibition, while increased I_{Kb} decreased $[Ca^{2+}]_i$. Ischemia caused an initial drop followed by a sustained rise in V_m. I_{Kb} activation caused an early hyperpolarisation of the membrane potential, which was subsequently countered by the depolarising effects of *NaK* inhibition, with acidosis having a limited effect.

Figure 4 plots the width of the BZ for each ion with striped bars corresponding to extracellular space and the darker the bar the more significant the concentration gradient relative to the initial concentration. This plot shows that $[K^+]_e$ had a significantly wider BZ with greater magnitude than $[Na^+]_i$. For pH regulation, H^+ had a narrower BZ compared to the significantly wider HCO_3^- BZ, which may indicate the facilitation of proton transport via HCO_3^- diffusion.

Extracellular Potassium Gradients

The $[K^+]_e$ BZ width was significantly wider than other BZ ion widths and notably larger than the $[Na^+]_i$ BZ width. To determine the cause of this extended $[K^+]_e$ BZ the source of the cumulative changes in $[K^+]_e$ due to transmembrane flux, drift or diffusion over the 5 minutes of ischemia were calculated and plotted in Fig. 5. This showed that only the transmembrane flux had a significant gradient across the ischemic region. Separating the transmembrane flux into the *NaK* and I_{Kb} components then identified the K^+ channel, which includes the ATP-inactivated K^+ current, as the cause of this gradient. The gradient of I_{Kb} was due to the extensive membrane potential gradient into the ischemic region (see Fig. 3). To confirm that this was the cause

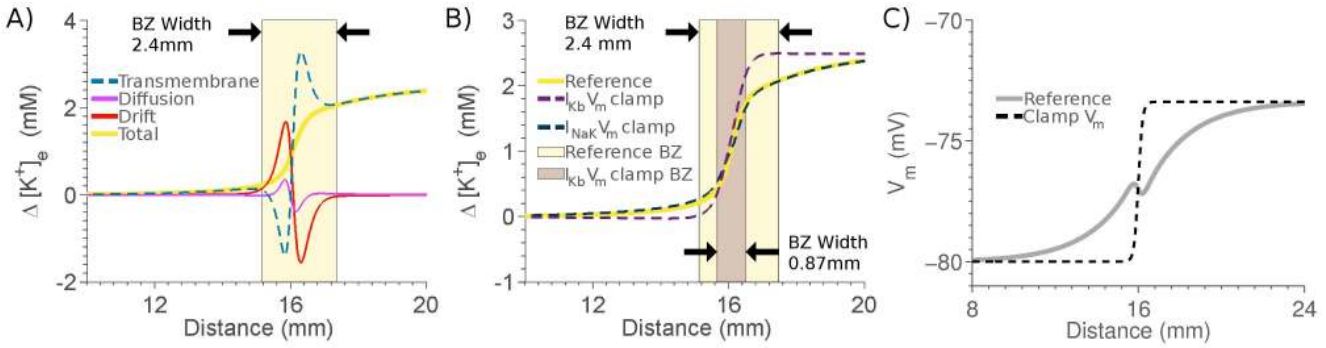

Figure 5. Mechanisms underpinning $[K^+]_e$ BZ width. A) Reference change in $[K^+]_e$ after 5 minutes of simulated ischemia caused by transmembrane flux (blue dashed line), diffusion (purple line), drift (red line) and the total change due to all causes (yellow line). The BZ is indicated by the yellow shaded region. B) Change in $[K^+]_e$ in the reference model (yellow line) compared with change in $[K^+]_e$ when I_{Kb} (purple dashed line) or NaK (blue dashed line) are exposed to a clamped membrane potential. The reference BZ and BZ when I_{Kb} is exposed to a clamped membrane potential are indicated by the yellow and purple shaded regions, respectively.
doi:10.1371/journal.pone.0060323.g005

of the $[K^+]_e$ BZ width, the membrane potential was calculated as normal, but an additional clamped membrane potential was calculated at each time step. The clamped membrane potential had the same maximum and minimum values as the correct membrane potential but instead of a smooth gradient across the BZ it had a sharp transition over the BZ. A comparison of this clamped and the control membrane potentials is shown in the Fig. 5C. The effects of using a clamped membrane potential to calculate the NaK flux or the I_{Kb} current on the cumulative changes in $[K^+]_e$ after 5 minutes of simulated ischemia are plotted in Fig. 5B, demonstrating that by removing the gradient in the membrane potential experienced by I_{Kb} there is a significant narrowing in the $[K^+]_e$ BZ.

Drift and Diffusion

To investigate the relative contribution of drift and diffusion to intra region fluxes (inter or extracellular) the drift and diffusion fluxes in each region were plotted, alongside the transmembrane flux, over the length of the strand after 5 minutes of ischemia. Fig. 6 shows the differences in drift and diffusion between Cl^-, Na^+ and K^+. As expected from the intra and extracellular gradients, intracellular K^+ and Cl^- diffused into and out of the ischemic region in the intra and extracellular space, respectively. The converse was the case for Na^+. Due to the decrease in transmembrane potential, characteristic of ischemic regions, there was a convergence of intra and extracellular potentials with the extracellular potential decreasing in the ischemic region and the intracellular potential increasing. This gradient caused positive ions to drift into the ischemic region in the extracellular space and drift out of the ischemic region in the intracellular space. The converse was true for negatively charged ions. As drift is proportional to the ionic concentration, Na^+ drift was significant in the extracellular space and K^+ drift was significant in the intracellular space. For Na^+, drift and diffusion operated in the same direction in the intra and extracellular space. The result was a cyclical movement of Na^+ moving into the ischemic region in the extracellular space, while moving out of the ischemic region in the intracellular space. The Cl^- movement was also circular but in the opposite direction (Fig. 6P). However, for K^+ drift and diffusion were in opposite directions. In the extracellular space where the K^+ concentration was low, diffusion dominated and K^+ moved out of the ischemic region. In the intracellular space, where there was a higher concentration of K^+, drift dominated, also causing K^+ ions to move out of the ischemic region. Thus ischemia caused a depletion of K^+ in the ischemic region through both the intra and extracellular space and, contrary to previous hypothesis [13], the model suggests that intracellular K^+ movement is the dominant path for K^+ to leave the ischemic region.

Discussion

In this study a new model of cardiac tissue electrophysiology was developed. The model predicted that the width of the $[K^+]_e$ gradient across an ischemic BZ would be significantly wider the $[Na^+]_i$ BZ. The cause of this difference was attributed to the voltage dependence of the I_{Kb} channel. The model also demonstrated that, due to electrogenic drift, K^+ moved out of the ischemic region in both the intra and extracellular space which will lead to K^+ depletion.

The model of ionic movement and tissue electrophysiology was developed by combining the Nernst-Plank equations with the bidomain framework. No attempt was made to explicitly validate the proposed tissue model equations due to the paucity of experimental data. However, applying simplifying assumptions with regards to ionic or voltage gradients reduces the proposed equations to the well validated bidomain equations [137,138] or coupled reaction-diffusion equations [28,86], respectively, providing support for the validity of the proposed modelling framework. The limited attempts at simulating the spatial temporal evolution of ionic gradients across the ischemic BZ have largely uncoupled the movement of ions and the electric field. Potse et al., [18] demonstrated that measured K^+ gradients across an ischemic BZ could be simulated using a model of K^+ diffusion coupled to a source term. The spatially varying $[K^+]_e$ gradient could then be included as a boundary condition to models of transmembrane current in the bidomain equations. This model did not include any effect of electric gradients on K^+ movement, $[K^+]_i$ movement, inter ionic species interactions or the effect of the ischemic region on any other ion gradient. Similar sets of equations to those proposed here have been used for simulating the potential gradient surrounding cells, including the Debye layer [139], electrical propagation along strands of cardiac cells [140,141] and for modelling ion diffusion in the cable equation [142]. These previous models have either explicitly represented the intra and extracellular domains or only considered the intracellular domain

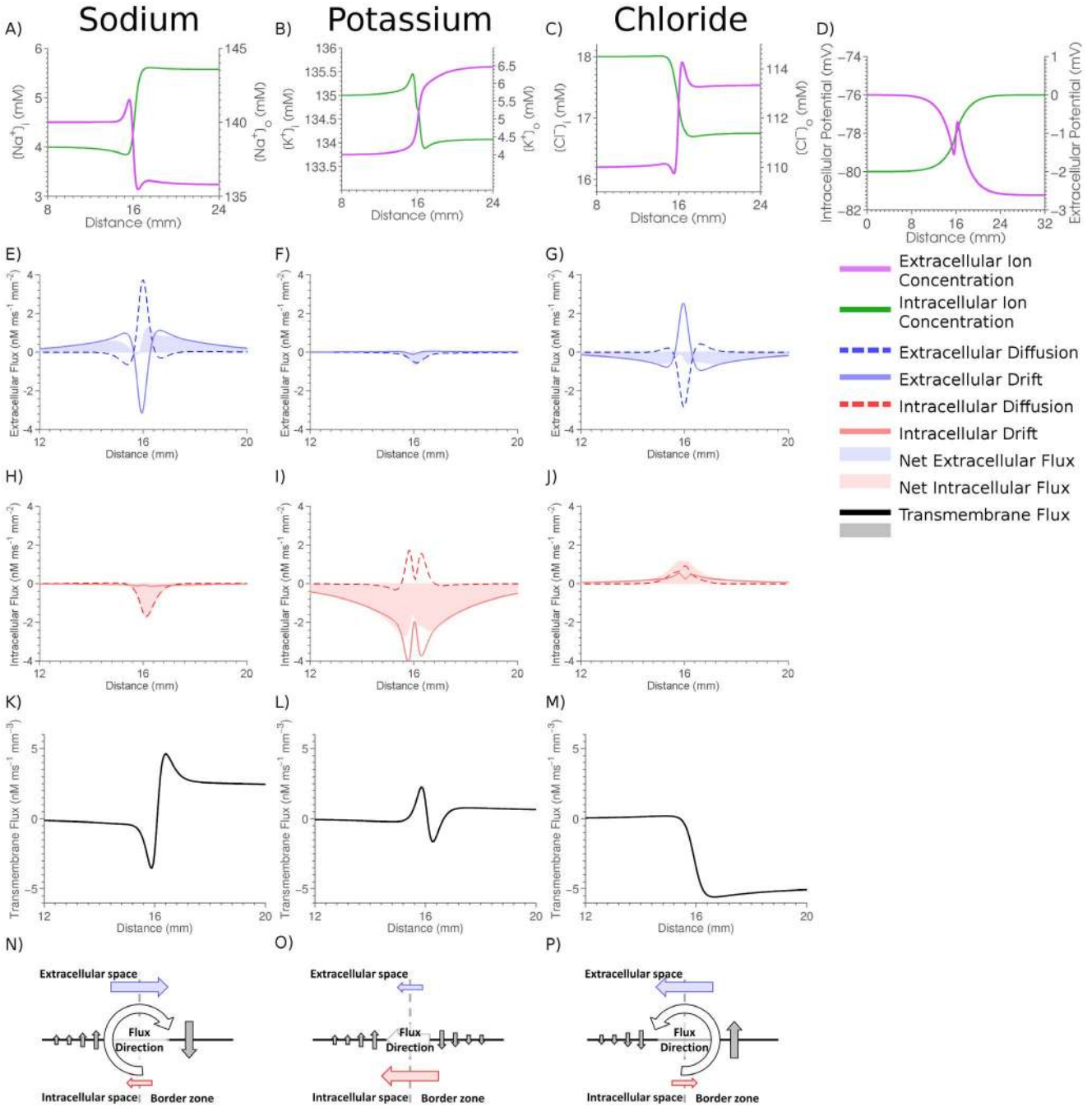

Figure 6. Regulation of Na^+, K^+ and Cl^- ionic concentrations across the border zone after 5 minutes of ischemia. Intra and extracellular A) Na^+, B) K^+ and C) Cl^- ionic concentrations. D) Intra and extracellular potential. Intracellular drift and diffusion flux of E) Na^+, F) K^+ and G) Cl^-. Extracellular drift and diffusion of H) Na^+, I) K^+ and J) Cl^-. Transmembrane flux of K) Na^+, L) K^+ and M) Cl^-. Schematics showing the general direction of ion movement within and between the intra and extracellular space for N) Na^+, O) K^+ and P) Cl^-.
doi:10.1371/journal.pone.0060323.g006

but have not modelled the tissue within the bidomain framework, as derived and implemented here.

The proposed equations can be applied generally in three dimensions as opposed to the one dimensional simulations presented here. The current study does not consider the effects of anisotropy on ion or membrane potential gradients across the BZ, however, if implemented in two or three dimensions the model is capable of representing tissue anisotropy and any effects this may have on BZ gradients. By conserving ionic species the proposed equations provide a more biophysical representation of cardiac electrophysiology than the bidomain equations and can appropriately be applied to simulate a broader range of conditions. However, these benefits come at a cost. Unlike the bidomain equations, with two partial differential equations that can readily be uncoupled and solved as two sets of linear equations [143], the proposed model is nonlinear and contains two parabolic partial differential equations for each ionic species and one elliptic partial differential equation to model the electric potential. This results in

a significant increase both in the complexity and number of equations that must be solved and hence comes at a significant increase in computational cost. The proposed framework can be used to simulate electrically active tissue by introducing a full action potential cell model [31]. This would require identifying and separating out the transmembrane pathways for each ionic species present in the cell model to calculate the net transmebrane flux for each ion or J_m^i in Eqn 18. The internal cell model state variables, including gating variables, Markov states and intracellular Ca^{2+} dynamics would also need to be solved, introducing a system of nonlinear ordinary differential equations at each grid point. The small time steps and increased number of degrees of freedom required to simulate electrically active tissue would further increase the computational cost of the proposed model.

A new model of ion movement across the un-stimulated cell membrane was developed. This model has been published online and is available at cellml.org. The model creation approach demonstrated two novel methods. Firstly, the ion transporter densities were uniquely constrained by a small number of experimental data sets and a zero net flux constraint. This provided a repeatable and unique method for determining model parameters under quiescent conditions and could readily be applied to any cardiac electrophysiology model to constrain model parameters. Secondly, in the development of this model a grid of 53 experimental observations were created to provide a comprehensive validation of the model response to changes in ion concentrations and in the presence of blockers of major transporters. Although these observations only provide a qualitative comparison, they do provide a benchmark for quantifying the generality of models. Furthermore, Table 4 identified 19 experiments that do not appear to have been performed or remain controversial, highlighting the potential for additional experiments.

In this study the process of validating the model against 53 experimental observations demonstrated the general capacity of the model to replicate the majority of experimental results. However, the model was unable to match ten of the 53 observations. Five of the experimental observations found no change in a measurement. Due to the numerical nature of the model, even very small changes in a concentration can be observed and without adding in a semi arbitrary threshold that should reflect the variability and confidence of each experimental measurement it was not possible for the model to return no change in a value. In general the five remaining failed observations can be attributed to absent mechanisms in the model or inconsistencies with the model and specific experimental setups. The model did not predict the $[Cl^-]_i$ response to depressed $[Na^+]_e$ and the $[K^+]_i$ response to depressed $[Cl^-]_e$. This is potentially due to the absence of NaK2Cl from the model, largely due to the lack of data characterising the transporter. The model was unable to replicate the decrease in V_m due to elevated $[Na^+]_e$. This may be due to the specifics of the experimental protocol. Decreasing $[Na^+]_e$, which should have the opposite effect on V_m, caused both increases and decreases in V_m in different studies indicating that the V_m dependence on $[Na^+]_e$ is sensitive to the specifics of the experimental setup. The model did not predict the change in V_m or H^+ with a decrease in $[Ca^{2+}]_e$. Experimental observations report an increase in V_m with both a decrease or an increase in $[Ca^{2+}]_e$. This may indicate that the V_m is at some minima with respect to $[Ca^{2+}]_e$, although this seems unlikely. It more likely reflects inconsistent data due to differences in experimental setups that were impossible for the model to replicate. In cardiac myocytes it is postulated that Ca^{2+} and H^+ compete for common buffering sites [144,145]. The decrease in $[Ca^{2+}]_e$ may drain the cell of Ca^{2+}, reducing the Ca^{2+} bound to buffers that could then be occupied by H^+, resulting in a decrease in $[H^+]_i$. A common pool of Ca^{2+} and H^+ buffering was not present in the model and this may explain the disparity between model predictions and experimental results. Despite the inability of the model to replicate 5 of the 53 observations, the majority of the absent mechanisms are expected to play a secondary role during ischemia. NaK2Cl is a potential contributor to the elevation in $[K^+]_e$ [146], although this has been questioned [131], and its absence is unlikely to affect the general model conclusions.

Models simulations found a BZ width for the different ions of between 0.3mm ($[Na^+]_e$) and 2.4mm ($[K^+]_e$). The variation in the width of each ion across the BZ means that there was no single BZ width predicted by the model. The majority of ions transitioned from viable to ischemic concentrations over $0.4-0.8$mm, with HCO_3^- and $[K^+]_e$ notable outliers. The model predictions are consistent with previous measurements of the BZ between 0.6 and 2mm [10,11,147–149]. However, the model did not include the sharp gradients in metabolites over 0.1mm [11] or the effects of regions of reduced perfusion affecting mechanics over 20 mm distance from the ischemic region [150].

The model predicted that $[K^+]_e$ and $[Na^+]_i$ have significantly different BZ widths (Fig. 4). It was expected that the coupling of $[Na^+]_i$ and $[K^+]_e$ via NaK would result in concordant gradients in these two ions across the BZ. The extended $[K^+]_e$ gradient was attributed to the voltage dependence of the I_{Kb} (Fig 5). Unlike $[Na^+]_i$, $[K^+]_e$ is regulated by two electrogenic transmembrane pathways I_{Kb} and NaK, whereas $[Na^+]_i$ is regulated by multiple exchangers that are electro neutral, or have attenuated voltage dependence, compared to ion channels. This discordance in $[Na^+]_i$ and $[K^+]_e$ gradients will have a significant effect on the gradient of action potential morphology across the BZ. Elevation of $[K^+]_e$ depolarises the cell and shortens the action potential duration, whereas elevation of $[Na^+]_i$ causes a reduction in action potential duration [151,152]. The combined effect of the two gradients will be a slower change in resting membrane potential on the length scale of the $[K^+]_e$ gradient and a much more rapid transition in action potential duration due to the faster change in $[Na^+]_i$ in conjunction with the change in $[K^+]_e$ over the BZ. The temporal evolution of the two gradients are also distinct, with a sustained constant increase in $[Na^+]_i$ over the first 5 minutes, while $[K^+]_e$ increases rapidly for 3 minutes before plateauing (Fig. 3). These simulation results are consistent with experimental measurements of ionic concentrations [111,152] and changes in ECG morphology, which report an early elevation of resting membrane potential, followed by a decrease in action potential duration [153] during early ischemia. These spatial-temporal increases in ion concentrations and secondary effects on electrophysiology will increase tissue heterogeneity and have the capacity to play an important role in the BZ arrhythmogenic substrate.

Experimental measurements have reported a decrease in $[K^+]_i$ during ischemia [152]. Loss of $[K^+]_i$ has been attributed to a combination of increased I_{Kb} conduction and NaK inhibition [152,154]. However, depletion of $[K^+]_i$ due to transmembrane K^+ movement, in the absence of a potential gradient, would cause an intracellular flux of K^+ into the ischemic zone, due to diffusion, to replenish $[K^+]_i$, mitigating the effects of changes of K^+ transmembrane flux on $[K^+]_i$. The model proposed here demonstrated that this is not necessarily the case. The model predicted a significant electrogenic K^+ flux in the intracellular space out of the ischemic zone (Fig. 6), resulting in a net efflux of

K^+ out of the ischemic zone both in the intra and extracellular space. The movement of K^+ in the intracellular space out of the ischemic zone would further deplete $[K^+]_i$ in the ischemic region and exacerbate $[K^+]_i$ loss, but may limit K^+ accumulation in the extracellular space.

Limitations

The model is inherently an approximation and hence represents a finite set of known cellular properties and changes that occur during ischemia. In particular, the model treated all buffers as static and rapid, the effects of protons on channel, exchanger and co-transports were not considered, ischemic changes were instantaneous and the model did not include all possible changes or pathways that may affect ionic homeostasis during ischemia.

The tissue model assumed that H^+ and Ca^{2+} buffers are static, rapid and made up of a single population of binding sites. It is known that some of the buffers for both H^+ and Ca^{2+} are mobile, these could be introduced into the model framework as an additional concentration but these effects were approximated, without the additional computational cost of adding a additional ionic concentration, by using effective diffusion constants. The equilibrium assumption was likely to be valid in the current model due to the long time scales of interest; however, simulation of cardiac action potentials would require the re-evaluation of this assumption. It is also known that H^+ [28] and Ca^{2+} [155] are buffered by multiple proteins with distinct binding kinetics but over the range of concentrations simulated these multiple buffer species were unlikely to have significant effects.

The model of intracellular Ca^{2+} dynamics assumes that the SR and cytosolic Ca^{2+} concentrations remain in equilibrium, which is clearly not the case during an action potential. The model of intracellular Ca^{2+} dynamics provided a numerically efficient representation of intracellular Ca^{2+} buffering and SR Ca^{2+} uptake. The use of a Hill coefficient of one for SERCA as opposed to the more common and biophysical value of two removed the need for an additional differential equation to model $[Ca^{2+}]_{SR}$ or the solution of a set of nonlinear equations to model Ca^{2+} regulation. Furthermore, over the range of Ca^{2+} values studied it was possible to adjust the maximum SERCA flux to minimize discrepancies between a model with a Hill coefficient of one or two.

It is well recognised that H^+ play an important role in regulating cellular electrophysiology [156]. Experimental and modelling studies have demonstrated the effects of H^+ on ryanodine receptor opening probabilities, NCX, Ca^{2+} channels, Ca^{2+} buffering and SERCA [22,157]. The majority of the effects of H^+ on $[Ca^{2+}]_i$ regulation are unlikely to play a significant role in determining the spatial and temporal K^+ and Na^+. However, inhibition of NCX potentially contributes to $[Na^+]_i$ gradients but this will be secondary to the effects of NaK inhibition.

The model treats all changes for ischemia as instantaneous. The time dependence of inhibition of NaK, activation of I_{Kb}, increased $[CO_2]_i$ flux or increased H^+ flux are not known and can only be approximated. A linear ramp in ischemic changes has been used previously, but this fails to consider the possibility that changes occur over different time scales. In order to minimise ambiguity in model simulations an instantaneous change in NaK, I_{Kb}, $[CO_2]_i$ flux and H^+ flux was chosen.

To limit the scope of this study, the effects of cell swelling and the effects of this on changes in ion concentrations [122] were not included in the model. However, previous, modelling studies have found these effects to not significantly alter $[K^+]_e$ accumulation and may not fundamentally alter the study conclusions [20]. Mitani and Shattock [146] identified the Na dependent potassium channel as a potential contributor to the elevation of $[K^+]_e$. However, the effects of an increase in any K^+ current are captured by the elevation in I_{Kb} that does not necessarily need to be the sole result of an increase in conduction in the ATP inactivated K^+ channel. Furthermore, the model does not include an increased Na^+ channel conductance during ischemia. This has been reported during ischemia in the form of increased permeability of Na^+ through the persistent Na^+ current [116] and the ATP activated K^+ channel [158]. However, other groups have found a limited impact of the persistent Na^+ channel in Na^+ accumulation during ischemia [159] and previous modelling studies have shown that its inclusion is not required to capture the salient features of ischemia in the single cell [20]. For these reasons a potential increase in the Na^+ channel conductance was not included in this study.

Summary

A new mathematical framework was derived for simulating cardiac tissue electrophysiology with ion species conservation. The model was used to simulate the movement of ions due to transmembrane channels, pumps and transporters, diffusion and drift in the intra and extracellular space. The model predicted that 1) the sodium BZ is approximately a quarter of the length of the potassium BZ and this is due to the effects of the membrane potential gradient on I_{Kb} and 2) that during ischemia there is a gross movement of potassium ions out of the ischemic region in both the intra and extracellular space due to the effects of drift, which will lead to a depletion of K^+ from the ischemic region.

Author Contributions

Conceived and designed the experiments: SAN. Performed the experiments: SAN. Analyzed the data: SAN. Contributed reagents/materials/analysis tools: SAN. Wrote the paper: SAN.

References

1. Kaplinsky E, Ogawa S, Balke CW, Dreifus LS (1979) Two periods of early ventricular arrhythmia in the canine acute myocardial infarction model. Circulation 60: 397–403.
2. Janse MJ, Cinca J, Morena H, Fiolet JW, Kleber AG, et al. (1979) The "border zone" in myocardial ischemia. an electrophysiological, metabolic, and histochemical correlation in the pig heart. Circulation Research 44: 576–588.
3. Cascio WE (2001) Myocardial ischemia: What factors determine arrhythmogenesis? Journal of Cardiovascular Electrophysiology 12: 726–729.
4. Zaitsev AV, Guha PK, Sarmast F, Kolli A, Berenfeld O, et al. (2003) Wavebreak formation during ventricular fibrillation in the isolated, regionally ischemic pig heart. Circulation Research 92: 546–553.
5. Carmeliet E (1999) Cardiac ionic currents and acute ischemia: From channels to arrhythmias. physiological reviews 73: 917–1017.
6. Sidorov VY, Uzelac I, Wikswo JP (2011) Regional increase of extracellular potassium leads to electrical instability and reentry occurrence through the spatial heterogeneity of apd restitution. American Journal of Physiology - Heart and Circulatory Physiology 301: H209–H220.
7. Weiss JN, Chen PS, Qu Z, Karagueuzian HS, Garfinkel A (2000) Ventricular fibrillation. Circulation Research 87: 1103–1107.
8. Horacek T, Neumann M, von Mutius S, Budden M, Meesmann W (1984) Nonhomogeneous electrophysiological changes and the bimodal distribution of early ventricular arrhythmias during acute coronary artery occlusion. Basic Research in Cardiology 79: 649–667.
9. Klber AG (1984) Extracellular potassium accumulation in acute myocardial ischemia. Journal of Molecular and Cellular Cardiology 16: 389–394.
10. Wilensky RL, Tranum-Jensen J, Coronel R, Wilde AA, Fiolet JW, et al. (1986) The subendocardial border zone during acute ischemia of the rabbit heart: an electrophysiologic, metabolic, and morphologic correlative study. Circulation 74: 1137–1146.

11. Harken AH, Barlow CH, Harden Iii WR, Chance B (1978) Two and three dimensional display of myocardial ischemic border zone in dogs. The American Journal of Cardiology 42: 954–959.
12. Yellon DM, Hearse DJ, Crome R, Grannell J, Wyse RKH (1981) Characterization of the lateral interface between normal and ischemic tissue in the canine heart during evolving myocardial infarction. The American Journal of Cardiology 47: 1233–1239.
13. Coronel R, Fiolet JW, Wilms-Schopman FJ, Schaapherder AF, Johnson TA, et al. (1988) Distribution of extracellular potassium and its relation to electrophysiologic changes during acute myocardial ischemia in the isolated perfused porcine heart. Circulation 77: 1125–1138.
14. Coronel R, Wilms-Schopman FJG, Fiolet JWT, Opthof T, Janse MJ (1995) The relation between extracellular potassium concentration and ph in the border zone during regional ischemia in isolated porcine hearts. Journal of Molecular and Cellular Cardiology 27: 2069–2073.
15. Tice BM, Rodrguez B, Eason J, Trayanova N (2007) Mechanistic investigation into the arrhythmogenic role of transmural heterogeneities in regional ischaemia phase 1a. Europace 9: vi46–vi58.
16. Trnor B, Ferrero JM, Rodrguez B, Montilla F (2005) Effects of pinacidil on reentrant arrhythmias generated during acute regional ischemia: A simulation study. Annals of Biomedical Engineering 33: 897–906.
17. Potse M, Coronel R, Falcao S, LeBlanc AR, Vinet A (2007) The effect of lesion size and tissue remodeling on ST deviation in partial-thickness ischemia. Heart Rhythm 4: 200–206.
18. Potse M, Coronel R, LeBlanc AR, Vinet A (2007) The role of extracellular potassium transport in computer models of the ischemic zone. Medical and Biological Engineering and Computing 45: 1187–1199.
19. Smith NP, Crampin EJ (2004) Development of models of active ion transport for whole-cell modelling: cardiac sodium-potassium pump as a case study. Progress in Biophysics & Molecular Biology 85: 387–405.
20. Terkildsen JR, Crampin EJ, Smith NP (2007) The balance between inactivation and activation of the Na^+-K^+ pump underlies the triphasic accumulation of extracellular K^+ during myocardial ischemia. Am J Physiol Heart Circ Physiol 293: H3036–3045.
21. Weber CR, Piacentino I Valentino, Ginsburg KS, Houser SR, Bers DM (2002) Na^+-Ca^{2+} exchange current and submembrane [Ca^{2+}]. during the cardiac action potential. Circulation Research 90: 182–189.
22. Crampin EJ, Smith NP (2006) A dynamic model of excitation-contraction coupling during acidosis in cardiac ventricular myocytes. Biophysical Journal 90: 3074–3090.
23. Niederer SA, Smith NP (2007) A mathematical model of the slow force response to stretch in rat ventricular myocytes. Biophysical Journal 92: 4030–44.
24. Wu ML, Vaughan-Jones RD (1997) Interaction between Na^+ and H^+ ions on Na-H exchange in sheep cardiac purkinje fibers. Journal of Molecular and Cellular Cardiology 29: 1131–1140.
25. Zaniboni M, Swietach P, Rossini A, Yamamoto T, Spitzer KW, et al. (2003) Intracellular proton mobility and buffering power in cardiac ventricular myocytes from rat, rabbit, and guinea pig. American Journal of Physiology 285: H1236–H1246.
26. Despa S, Islam MA, Pogwizd SM, Bers DM (2002) Intracellular Na^+. and Na^+ pump rate in rat and rabbit ventricular myocytes. J Physiol (Lond) 539: 133–143.
27. Niederer SA, Swietach P, Wilson DA, Smith NP, Vaughan-Jones RD (2008) Measuring and modeling chloride-hydroxyl exchange in the guinea-pig ventricular myocyte. Biophysical Journal 94: 2385–403.
28. Zaniboni M, Rossini A, Swietach P, Banger N, Spitzer KW, et al. (2003) Proton permeation through the myocardial gap junction. Circulation Research 93: 726–735.
29. Faber GM, Rudy Y (2000) Action potential and contractility changes in Na^+ (i) overloaded cardiac myocytes: A simulation study. Biophysical Journal 78: 2392–2404.
30. Komukai K, Brette F, Pascarel C, Orchard CH (2002) Electrophysiological response of rat ventricular myocytes to acidosis. American Journal of Physiology - Heart and Circulatory Physiology 283: H412–H422.
31. Fink M, Niederer SA, Cherry EM, Fenton FH, Koivumki JT, et al. (2011) Cardiac cell modelling: Observations from the heart of the cardiac physiome project. Progress in Biophysics and Molecular Biology 104: 2–21.
32. Monnereau-Soustre H, Revial MF, Lcoty C, Pager J (1969) evaluation of extracellular space of the rat heart: effect of adrenalectomy; electrophysiological implications. C R Seances Soc Biol Fil 163: 1419–22.
33. Polimeni P (1974) Extracellular space and ionic distribution in rat ventricle. American Journal of Physiology – Legacy Content 227: 676–683.
34. Poole-Wilson P, Cameron I (1975) ECS, intracellular pH, and electrolytes of cardiac and skeletal muscle. American Journal of Physiology – Legacy Content 229: 1299–1304.
35. Caille JP, Ruiz-Ceretti E, Schanne OF (1981) Intracellular chloride activity in rabbit papillary muscle: effect of ouabain. American Journal of Physiology - Cell Physiology 240: C183–C188.
36. Polimeni PI (1974) Cardiac electrolytes and water in thyroparathyroidectomized rat. Journal of Molecular and Cellular Cardiology 6: 531–541.
37. Page E (1978) Quantitative ultrastructural analysis in cardiac membrane physiology. American Journal of Physiology - Cell Physiology 235: C147–C158.
38. Page E, Surdyk-Droske M (1979) Distribution, surface density, and membrane area of diadic junctional contacts between plasma membrane and terminal cisterns in mammalian ventricle. Circulation Research 45: 260–267.
39. Chopra N, Kannankeril PJ, Yang T, Hlaing T, Holinstat I, et al. (2007) Modest reductions of cardiac calsequestrin increase sarcoplasmic reticulum Ca^{2+} leak independent of luminal Ca^{2+} and trigger ventricular arrhythmias in mice. Circulation Research 101: 617–626.
40. Singh S, White F, Bloor C (1981) Myocardial morphometric characteristics in swine. Circulation Research 49: 434–441.
41. Abete P, Vassalle M (1988) Relation between Na^+-K^+ pump, Na^+ activity and force in strophanthidin inotropy in sheep cardiac purkinje fibres. The Journal of Physiology 404: 275–299.
42. Sossalla S, Wagner S, Rasenack ECL, Ruff H, Weber SL, et al. (2008) Ranolazine improves diastolic dysfunction in isolated myocardium from failing human hearts – role of late sodium current and intracellular ion accumulation. Journal of Molecular and Cellular Cardiology 45: 32–43.
43. Kimura S, Bassett AL, Gaide MS, Kozlovskis PL, Myerburg RJ (1986) Regional changes in intracellular potassium and sodium activity after healing of experimental myocardial infarction in cats. Circulation Research 58: 202–208.
44. Baartscheer A, Hardziyenka M, Schumacher CA, Belterman CNW, Borren MMGJv, et al. (2008) Chronic inhibition of the Na-H exchanger causes regression of hypertrophy, heart failure, and ionic and electrophysiological remodelling. British Journal of Pharmacology 154: 1266–1275.
45. Lee CO, Fozzard HA (1975) Activities of potassium and sodium ions in rabbit heart muscle. The Journal of General Physiology 65: 695–708.
46. Prasad K, Khatter JC, Bharadwaj B (1979) Intra- and extracellular electrolytes and sarcolemmal ATPase in the failing heart due to pressure overload in dogs. Cardiovascular Research 13: 95–104.
47. Cohen C, Fozzard H, Sheu S (1982) Increase in intracellular sodium ion activity during stimulation in mammalian cardiac muscle. Circulation Research 50: 651–662.
48. Baumgarten CM, Fozzard HA (1981) Intracellular chloride activity in mammalian ventricular muscle. American Journal of Physiology - Cell Physiology 241: C121–C129.
49. Powell T, Terrar DA, Twist VW (1980) Electrical properties of individual cells isolated from adult rat ventricular myocardium. The Journal of Physiology 302: 131–153.
50. Vaughan-Jones RD (1979) Non-passive chloride distribution in mammalian heart muscle: micro-electrode measurement of the intracellular chloride activity. The Journal of Physiology 295: 83–109.
51. Lai ZF, Nishi K (1998) Intracellular chloride activity increases in guinea pig ventricular muscle during simulated ischemia. American Journal of Physiology - Heart and Circulatory Physiology 275: H1613–H1619.
52. Bers DM (2001) excitation-contraction coupling and cardiac contractile force. Dordrecht: Kluwer Academic Publishers, first edition.
53. Baartscheer A, Schumacher CA, Belterman CN, Coronel R, Fiolet JW (2003) SR calcium handling and calcium after-transients in a rabbit model of heart failure. Cardiovascular Research 58: 99–108.
54. Bassani JW, Bassani RA, Bers DM (1995) Calibration of indo-1 and resting intracellular [Ca]$_i$ in intact rabbit cardiac myocytes. Biophysical Journal 68: 1453–1460.
55. Siri FM, Krueger J, Nordin C, Ming Z, Aronson RS (1991) Depressed intracellular calcium transients and contraction in myocytes from hypertrophied and failing guinea pig hearts. American Journal of Physiology - Heart and Circulatory Physiology 261: H514–H530.
56. Han S, Schiefer A, Isenberg G (1994) Ca^{2+} load of guinea-pig ventricular myocytes determines efficacy of brief Ca^{2+} currents as trigger for Ca^{2+} release. The Journal of Physiology 480: 411–421.
57. Nakanishi T, Seguchi M, Tsuchiya T, Yasukouchi S, Takao A (1990) Effect of acidosis on intracellular ph and calcium concentration in the newborn and adult rabbit myocardium. Circulation Research 67: 111–123.
58. Terracciano CM, MacLeod KT (1997) Measurements of Ca^{2+} entry and sarcoplasmic reticulum Ca^{2+} content during the cardiac cycle in guinea pig and rat ventricular myocytes. Biophysical journal 72: 1319–1326.
59. Varro A, Negretti N, Hester SB, Eisner DA (1993) An estimate of the calcium content of the sarcoplasmic reticulum in rat ventricular myocytes. Pflügers Archiv European Journal of Physiology 423: 158–160.
60. Bassani RA, Bers DM (1995) Rate of diastolic Ca release from the sarcoplasmic reticulum of intact rabbit and rat ventricular myocytes. Biophysical Journal 68: 2015–2022.
61. Delbridge LM, Satoh H, Yuan W, Bassani JW, Qi M, et al. (1997) Cardiac myocyte volume, Ca^{2+} fluxes, and sarcoplasmic reticulum loading in pressure-overload hypertrophy. American Journal of Physiology - Heart and Circulatory Physiology 272: H2425–H2435.
62. Hobai IA, ORourke B (2001) Decreased sarcoplasmic reticulum calcium content is responsible for defective excitation-contraction coupling in canine heart failure. Circulation 103: 1577–1584.
63. Trafford AW, Daz ME, Eisner DA (1999) A novel, rapid and reversible method to measure ca buffering and time-course of total sarcoplasmic reticulum ca content in cardiac ventricular myocytes. Pflgers Archiv European Journal of Physiology 437: 501–503.
64. Bennett DL, ONeill SC, Eisner DA (1999) Strophanthidin-induced gain of Ca^{2+} occurs during diastole and not systole in guinea-pig ventricular myocytes. Pflugers Archiv European Journal of Physiology 437: 731–736.

65. Hove-Madsen L, Bers D (1993) Sarcoplasmic reticulum Ca^{2+} uptake and thapsigargin sensitivity in permeabilized rabbit and rat ventricular myocytes. Circulation Research 73: 820–828.
66. Berlin JR, Bassani JW, Bers DM (1994) Intrinsic cytosolic calcium buffering properties of single rat cardiac myocytes. Biophysical Journal 67: 1775–1787.
67. Walden AP, Dibb KM, Trafford AW (2009) Differences in intracellular calcium homeostasis between atrial and ventricular myocytes. Journal of Molecular and Cellular Cardiology 46: 463–473.
68. Díaz ME, Trafford AW, Eisner DA (2001) The effects of exogenous calcium buffers on the systolic calcium transient in rat ventricular myocytes. Biophysical Journal 80: 1915–1925.
69. Gottlieb RA, Gruol DL, Zhu JY, Engler RL (1996) Preconditioning rabbit cardiomyocytes: role of ph, vacuolar proton atpase, and apoptosis. J Clin Invest 97: 2391–8.
70. Leem CH, Lagadic-Gossmann D, Vaughan-Jones RD (1999) Characterization of intracellular pH regulation in the guinea-pig ventricular myocyte. Journal of Physiology 517: 159–180.
71. Lagadic-Gossmann D, Buckler KJ, Vaughan-Jones RD (1992) Role of bicarbonate in pH recovery from intracellular acidosis in the guinea-pig ventricular myocyte. Journal of Physiology 458: 361–384.
72. Cummings JR (1960) Electrolyte changes in heart tissue and coronary arterial and venous plasma following coronary occlusion. Circulation Research 8: 865–870.
73. Polimeni P, Al-Sadir J (1975) Expansion of extracellular space in the nonischemic zone of the infarcted heart and concomitant changes in tissue electrolyte contents in the rat. Circulation Research 37: 725–732.
74. Boyer PK, Poindexter CA (1940) The influence of digitalis on the electrolyte and water balance of heart muscle. American Heart Journal 20: 586–591.
75. Erdmann E, Bolte HD, Lderitz B (1971) The $(Na^+ + K^+)$-atpase activity of guinea pig heart muscle in potassium deficiency. Archives of Biochemistry and Biophysics 145: 121–125.
76. Kunze D (1977) Rate-dependent changes in extracellular potassium in the rabbit atrium. Circulation Research 41: 122–127.
77. Moore EW (1970) Ionized calcium in normal serum, ultrafiltrates, and whole blood determined by ion-exchange electrodes. J Clin Invest 49: 318–34.
78. Post JA, Langer GA (1992) Sarcolemmal calcium binding sites in heart: I. molecular origin in "gas-dissected" sarcolemma. Journal of Membrane Biology 129: 49–57.
79. Bers DM, Philipson KD, Langer GA (1981) Cardiac contractility and sarcolemmal calcium binding in several cardiac muscle preparations. American Journal of Physiology - Heart and Circulatory Physiology 240: H576–H583.
80. Gayeski TE, Honig CR (1991) Intracellular PO_2 in individual cardiac myocytes in dogs, cats, rabbits, ferrets, and rats. American Journal of Physiology - Heart and Circulatory Physiology 260: H522–H531.
81. Yan G, Kleber A (1992) Changes in extracellular and intracellular ph in ischemic rabbit papillary muscle. Circulation Research 71: 460–470.
82. Leem CH, Vaughan-Jones RD (1998) Sarcolemmal mechanisms for pH(i) recovery from alkalosis in the guinea-pig ventricular myocyte. Journal of Physiology 509: 487–496.
83. Austin WH, Lacombe E, Rand PW, Chatterjee M (1963) Solubility of carbon dioxide in serum from 15 to 38 c. Journal of Applied Physiology 18: 301–304.
84. Conway RS, Weiss HR (1985) Dependence of spatial heterogeneity of myocardial blood flow on mean blood flow rate in the rabbit heart. Cardiovascular Research 19: 160–168.
85. Despa S, Bers DM (2003) Na/K pump current and $Na._i$ in rabbit ventricular myocytes: Local $Na._i$ depletion and Na buffering. Biophysical Journal 84: 4157–4166.
86. Swietach P, Zaniboni M, Stewart AK, Rossini A, Spitzer KW, et al. (2003) Modelling intracellular H^+ ion diffusion. Progress in Biophysics and Molecular Biology 83: 69–100.
87. Bassani JW, Bassani RA, Bers DM (1994) Relaxation in rabbit and rat cardiac cells: species-dependent differences in cellular mechanisms. The Journal of Physiology 476: 279–293.
88. Balke CW, Egan TM, Wier WG (1994) Processes that remove calcium from the cytoplasm during excitation-contraction coupling in intact rat heart cells. The Journal of Physiology 474: 447–462.
89. Shannon TR, Ginsburg KS, Bers DM (2002) Quantitative assessment of the SR Ca^{2+} leak-load relationship. Circulation Research 91: 594–600.
90. Zima AV, Bovo E, Bers DM, Blatter LA (2010) Ca^{2+} spark-dependent and -independent sarcoplasmic reticulum Ca^{2+} leak in normal and failing rabbit ventricular myocytes. The Journal of Physiology 588: 4743–4757.
91. Li L, Niederer SA, Idigo W, Zhang YH, Swietach P, et al. (2010) A mathematical model of the murine ventricular myocyte: a data-driven biophysically based approach applied to mice overexpressing the canine NCX isoform. Am J Physiol Heart Circ Physiol 299: H1045–63.
92. Mattiazzi A, Hove-Madsen L, Bers DM (1994) Protein kinase inhibitors reduce SR Ca transport in permeabilized cardiac myocytes. American Journal of Physiology - Heart and Circulatory Physiology 267: H812–H820.
93. Roth BJ (1997) Electrical conductivity values used with the bidomain model of cardiac tissue. Biomedical Engineering, IEEE Transactions on 44: 326–328.
94. Cordeiro JM, Spitzer KW, Giles WR, Ershler PE, Cannell MB, et al. (2001) Location of the initiation site of calcium transients and sparks in rabbit heart purkinje cells. The Journal of Physiology 531: 301–314.
95. Kitazawa T (1984) Effect of extracellular calcium on contractile activation in guinea-pig ventricular muscle. The Journal of Physiology 355: 635–659.
96. Backx PH, de Tombe PP, Van Deen JH, Mulder BJ, ter Keurs HE (1989) A model of propagating calcium-induced calcium release mediated by calcium diffusion. The Journal of General Physiology 93: 963–977.
97. Cascio W, Yan G, Kleber A (1992) Early changes in extracellular potassium in ischemic rabbit myocardium. the role of extracellular carbon dioxide accumulation and diffusion. Circulation Research 70: 409–422.
98. Swietach P, Rossini A, Spitzer KW, Vaughan-Jones RD (2007) H^+ ion activation and inactivation of the ventricular gap junction: A basis for spatial regulation of intracellular pH. Circulation Research 100: 1045–1054.
99. Rodriguez B, Tice BM, Eason JC, Aguel F, Ferrero J Jose M, et al. (2004) Effect of acute global ischemia on the upper limit of vulnerability: a simulation study. Am J Physiol Heart Circ Physiol 286: H2078–2088.
100. Dennis SC, Gevers W, Opie LH (1991) Protons in ischemia: Where do they come from; where do they go to? Journal of Molecular and Cellular Cardiology 23: 1077–1086.
101. Bonen A (2001) The expression of lactate transporters (MCT1 and MCT4) in heart and muscle. European Journal of Applied Physiology 86: 6–11.
102. Vinnakota KC, Beard DA (2011) Kinetic analysis and design of experiments to identify the catalytic mechanism of the monocarboxylate transporter isoforms 4 and 1. Biophysical Journal 100: 369–380.
103. Wang YP, Fuchs F (1994) Length, force, and Ca^{2+}-troponin-C affinity in cardiac and slow skeletal-muscle. American Journal of Physiology 266: C1077–C1082.
104. Hak JB, van Beek JH, van Wijhe MH, Westerhof N (1993) Dynamics of myocardial lactate efflux after a step in heart rate in isolated rabbit hearts. American Journal of Physiology - Heart and Circulatory Physiology 265: H2081–H2085.
105. Rumsey WL, Pawlowski M, Lejavardi N, Wilson DF (1994) Oxygen pressure distribution in the heart in vivo and evaluation of the ischemic "border zone". Am J Physiol Heart Circ Physiol 266: H1676–1680.
106. Khuri SF, Flaherty JT, O'Riordan JB, Pitt B, Brawley RK, et al. (1975) Changes in intramyocardial st segment voltage and gas tensions with regional myocardial ischemia in the dog. Circulation Research 37: 455–63.
107. Hillis LD, Khuri SF, Braunwald E, Kloner RA, Tow D, et al. (1979) Assessment of the efficacy of interventions to limit ischemic injury by direct measurement of intramural carbon dioxide tension after coronary artery occlusion in the dog. The Journal of Clinical Investigation 63: 99–107.
108. Park CO, Xiao XH, Allen DG (1999) Changes in intracellular Na^+ and pH in rat heart during ischemia: role of Na^+/H^+ exchanger. Am J Physiol Heart Circ Physiol 276: H1581–1590.
109. Elliott AC, Smith GL, Eisner DA, Allen DG (1992) Metabolic changes during ischaemia and their role in contractile failure in isolated ferret hearts. The Journal of Physiology 454: 467–490.
110. Wilde AA, Escande D, Schumacher CA, Thuringer D, Mestre M, et al. (1990) Potassium accumulation in the globally ischemic mammalian heart. a role for the atp-sensitive potassium channel. Circulation Research 67: 835–43.
111. Pike MM, Luo CS, Clark MD, Kirk KA, Kitakaze M, et al. (1993) NMR measurements of Na^+ and cellular energy in ischemic rat heart: role of Na^+-H^+ exchange. Am J Physiol Heart Circ Physiol 265: H2017–2026.
112. Ten Hove M, Nederhoff MGJ, Van Echteld CJA (2005) Relative contributions of Na^+/H^+ exchange and Na^+/HCO_3^- cotransport to ischemic Na_i^+ overload in isolated rat hearts. Am J Physiol Heart Circ Physiol 288: H287–292.
113. van Echteld CJA, Kirkels JH, Eijgelshoven MHJ, van der Meer P, Ruigrok TJC (1991) Intracellular sodium during ischemia and calcium-free perfusion: A 23Na NMR study. Journal of Molecular and Cellular Cardiology 23: 297–307.
114. Imahashi K, Kusuoka H, Hashimoto K, Yoshioka J, Yamaguchi H, et al. (1999) Intracellular sodium accumulation during ischemia as the substrate for reperfusion injury. Circulation Research 84: 1401–1406.
115. Van Emous JG, Vleggeert-Lankamp CLAM, Nederhoff MGJ, Ruigrok TJC, Van Echteld CJA (2001) Postischemic Na^+-K^+-ATPase reactivation is delayed in the absence of glycolytic ATP in isolated rat hearts. Am J Physiol Heart Circ Physiol 280: H2189–2195.
116. Xiao XH, Allen DG (1999) Role of Na^+/H^+ exchanger during ischemia and preconditioning in the isolated rat heart. Circulation Research 85: 723–730.
117. El Banani H, Bernard M, Baetz D, Cabanes E, Cozzone P, et al. (2000) Changes in intracellular sodium and ph during ischaemia–reperfusion are attenuated by trimetazidine. Cardiovascular Research 47: 688–696.
118. Imahashi K, Nishimura T, Yoshioka J, Kusuoka H (2001) Role of intracellular Na^+ kinetics in preconditioned rat heart. Circulation Research 88: 1176–1182.
119. Baetz D, Bernard M, Pinet C, Tamareille S, Chattou S, et al. (2003) Different pathways for sodium entry in cardiac cells during ischemia and early reperfusion. Molecular and Cellular Biochemistry 242: 115–120.
120. Kleber A (1983) Resting membrane potential, extracellular potassium activity, and intracellular sodium activity during acute global ischemia in isolated perfused guinea pig hearts. Circulation Research 52: 442–450.
121. Hartmann M, Decking UKM (1999) Blocking Na^+-H^+ exchange by cariporide reduces Na^+-overload in ischemia and is cardioprotective. Journal of Molecular and Cellular Cardiology 31: 1985–1995.
122. Yan GX, Chen J, Yamada KA, Klber AG, Corr PB (1996) Contribution of shrinkage of extracellular space to extracellular K^+ accumulation in myocardial ischaemia of the rabbit. The Journal of Physiology 490: 215–228.

123. Vanheel B, Hemptinne Ad (1992) Influence of K_{ATP} channel modulation on net potassium efflux from ischaemic mammalian cardiac tissue. Cardiovascular Research 26: 1030–1039.
124. Hill J, Gettes L (1980) Effect of acute coronary artery occlusion on local myocardial extracellular K^+ activity in swine. Circulation 61: 768–778.
125. Kanda A, Watanabe I, Williams ML, Engle CL, Li S, et al. (1997) Unanticipated lessening of the rise in extracellular potassium during ischemia by pinacidil. Circulation 95: 1937–1944.
126. Mitani A, Kinoshita K, Fukamachi K, Sakamoto M, Kurisu K, et al. (1991) Effects of glibenclamide and nicorandil on cardiac function during ischemia and reperfusion in isolated perfused rat hearts. Am J Physiol Heart Circ Physiol 261: H1864–1871.
127. Wiegand V, Guggi M, Meesmann W, Kessler M, Greitschus F (1979) Extracellular potassium activity changes in the canine myocardium after acute coronary occlusion and the influence of beta-blockade. Cardiovascular Research 13: 297–302.
128. Yan GX, Joshi A, Guo D, Hlaing T, Martin J, et al. (2004) Phase 2 reentry as a trigger to initiate ventricular fibrillation during early acute myocardial ischemia. Circulation 110: 1036–1041.
129. Kimura J, Miyamae S, Noma A (1987) Identification of sodium calcium exchange current in single ventricular cells of guinea-pig. Journal of Physiology-London 384: 199–222.
130. Kimura S, Bassett AL, Kohya T, Kozlovskis PL, Myerburg RJ (1986) Simultaneous recording of action potentials from endocardium and epicardium during ischemia in the isolated cat ventricle: relation of temporal electrophysiologic heterogeneities to arrhythmias. Circulation 74: 401–409.
131. Gasser RN, Vaughan-Jones RD (1990) Mechanism of potassium efflux and action potential shortening during ischaemia in isolated mammalian cardiac muscle. The Journal of Physiology 431: 713–741.
132. Cole WC, McPherson CD, Sontag D (1991) ATP-regulated K^+ channels protect the myocardium against ischemia/reperfusion damage. Circulation Research 69: 571–81.
133. Saito T, Sato T, Miki T, Seino S, Nakaya H (2005) Role of ATP-sensitive K^+ channels in electrophysiological alterations during myocardial ischemia: a study using kir6.2-null mice. American Journal of Physiology - Heart and Circulatory Physiology 288: H352–H357.
134. Rouet R, Picard S, Libersa C, Ghadanfar M, Alabaster C, et al. (2000) Electrophysiological effects of dofetilide in an in vitro model of ''border zone'' between normal and ischemic/reperfused myocardium. Circulation 101: 86–93.
135. Yvon A, Hanouz J, Terrien X, Ducouret P, Rouet R, et al. (2002) Electrophysiological effects of morphine in an in vitro model of the 'border zone' between normal and ischaemic–reperfused guinea-pig myocardium. British Journal of Anaesthesia 89: 888–895.
136. Ducroq J, Rouet R, Puddu PE, Sall L, Tabourel C, et al. (2005) Electrophysiological effects of azimilide in an in vitro model of simulated-ischemia and reperfusion in guinea-pig ventricular myocardium. European Journal of Pharmacology 518: 165–174.
137. Wikswo Jr JP, Lin SF, Abbas RA (1995) Virtual electrodes in cardiac tissue: a common mechanism for anodal and cathodal stimulation. Biophysical Journal 69: 2195–2210.
138. Muzikant AL, Henriquez CS (1998) Validation of three-dimensional conduction models using experimental mapping: are we getting closer? Progress in Biophysics & Molecular Biology 69: 205–223.
139. Richardson G (2009) A multiscale approach to modelling electrochemical processes occurring across the cell membrane with application to transmission of action potentials. Mathematical Medicine and Biology.
140. Mori Y, Fishman GI, Peskin CS (2008) Ephaptic conduction in a cardiac strand model with 3D electrodiffusion. Proceedings of the National Academy of Sciences 105: 6463–6468.
141. Hand P, Peskin C (2010) Homogenization of an electrophysiological model for a strand of cardiac myocytes with gap-junctional and electric-field coupling. Bulletin of Mathematical Biology 72: 1408–1424.
142. Nygren A, Halter JA (1999) A general approach to modeling conduction and concentration dynamics in excitable cells of concentric cylindrical geometry. Journal of Theoretical Biology 199: 329–358.
143. Vigmond EJ, Aguel F, Trayanova NA (2002) Computational techniques for solving the bidomain equations in three dimensions. Biomedical Engineering, IEEE Transactions on 49: 1260–1269.
144. Blanchard E, Solaro R (1984) Inhibition of the activation and troponin calcium binding of dog cardiac myofibrils by acidic ph. Circulation Research 55: 382–391.
145. Orchard CH, Kentish JC (1990) Effects of changes of pH on the contractile function of cardiac-muscle. American Journal of Physiology 258: C967–C981.
146. Mitani A, Shattock MJ (1992) Role of Na-activated K channel, Na-K-Cl cotransport, and Na-K pump in $[K]_c$ changes during ischemia in rat heart. Am J Physiol Heart Circ Physiol 263: H333–340.
147. Coronel R, Wilms-Schopman FJ, Opthof T, van Capelle FJ, Janse MJ (1991) Injury current and gradients of diastolic stimulation threshold, TQ potential, and extracellular potassium concentration during acute regional ischemia in the isolated perfused pig heart. Circulation Research 68: 1241–9.
148. Hearse DJ, Yellon DM (1981) The border zone in evolving myocardial infarction: Controversy or confusion? The American Journal of Cardiology 47: 1321–1334.
149. Schaapherder AFM, Schumacher CA, Coronel R, Fiolet JWT (1990) Transmural inhomogeneity of extracellular K. and pH and myocardial energy metabolism in the isolated rat heart during acute global ischemia; dependence on gaseous environment. Basic Research in Cardiology 85: 33–44.
150. Prinzen FW, Arts T, Hoeks APG, Reneman RS (1989) Discrepancies between myocardial blood flow and fiber shortening in the ischemic border zone as assessed with video mapping of epicardial deformation. Pflügers Archiv European Journal of Physiology 415: 220–229.
151. Carmeliet E (2006) Action potential duration, rate of stimulation, and intracellular sodium. Journal of Cardiovascular Electrophysiology 17: S2–S7.
152. Wilde AA, Aksnes G (1995) Myocardial potassium loss and cell depolarisation in ischaemia and hypoxia. Cardiovascular Research 29: 1–15.
153. Kleber AG, Janse MJ, van Capelle FJ, Durrer D (1978) Mechanism and time course of S-T and T-Q segment changes during acute regional myocardial ischemia in the pig heart determined by extracellular and intracellular recordings. Circulation Research 42: 603–613.
154. Kantor PF, Coetzee WA, Carmeliet EE, Dennis SC, Opie LH (1990) Reduction of ischemic K^+ loss and arrhythmias in rat hearts. effect of glibenclamide, a sulfonylurea. Circulation Research 66: 478–85.
155. Robertson SP, Johnson JD, Potter JD (1981) The time-course of Ca^{2+} exchange with calmodulin, troponin, parvalbumin, and myosin in response to transient increases in Ca^{2+}. Biophysical Journal 34: 559–569.
156. Allen DG, Orchard CH (1983) The effects of changes of pH on intracellular calcium transients in mammalian cardiac-muscle. Journal of Physiology 335: 555–567.
157. Vaughan-Jones RD, Spitzer KW, Swietach P (2009) Intracellular pH regulation in heart. Journal of Molecular and Cellular Cardiology 46: 318–331.
158. Bollensdorff C, Knopp A, Biskup C, Zimmer T, Benndorf K (2004) Na+ current through katp channels: consequences for Na^+ and K^+ fluxes during early myocardial ischemia. Am J Physiol Heart Circ Physiol 286: H283–295.
159. Eigel BN, Hadley RW (1999) Contribution of the Na^+ channel and Na^+/H^+ exchanger to the anoxic rise of Na^+. in ventricular myocytes. American Journal of Physiology 277: H1817–1822.
160. Ellis D (1977) Effects of external cations and ouabain on intracellular sodium activity of sheep heart purkinje-fibers. Journal of Physiology-London 273: 211–240.
161. Deitmer JW, Ellis D (1980) Interactions between the regulation of the intracellular pH and sodium activity of sheep cardiac purkinje fibres. The Journal of Physiology 304: 471–488.
162. Bers DM, Ellis D (1982) Intracellular calcium and sodium activity in sheep heart purkinje-fibers - effect of changes of external sodium and intracellular pH. Pfluegers Archiv European Journal of Physiology 393: 171–178.
163. Katzung B (1975) Effects of extracellular calcium and sodium on depolarization-induced automaticity in guinea pig papillary muscle. Circulation Research 37: 118–127.
164. Baartscheer A, Schumacher CA, Fiolet JWT (1997) Small changes of cytosolic sodium in rat ventricular myocytes measured with SBFI in emission ratio mode. Journal of Molecular and Cellular Cardiology 29: 3375–3383.
165. Vaughan-Jones RD, Wu ML (1990) Extracellular H^+ inactivation of Na^+-H^+ exchange in the sheep cardiac purkinje fibre. Journal of Physiology 428: 441–466.
166. Ellis D, MacLeod KT (1985) Sodium-dependent control of intracellular pH in purkinje fibres of sheep heart. The Journal of Physiology 359: 81–105.
167. Kusuoka H, de Hurtado MCC, Marban E (1993) Role of sodium/calcium exchange in the mechanism of myocardial stunning: Protective effect of reperfusion with high sodium solution. Journal of the American College of Cardiology 21: 240–248.
168. Sasyniuk BI, Jhamandas V (1984) Mechanism of reversal of toxic effects of amitriptyline on cardiac purkinje fibers by sodium bicarbonate. Journal of Pharmacology and Experimental Therapeutics 231: 387–394.
169. Cheung JY, Thompson IG, Bonventre JV (1982) Effects of extracellular calcium removal and anoxia on isolated rat myocytes. American Journal of Physiology - Cell Physiology 243: C184–C190.
170. Kaila K, Vaughan-Jones RD (1987) Influence of sodium-hydrogen exchange on intracellular pH, sodium and tension in sheep cardiac purkinje fibres. The Journal of Physiology 390: 93–118.
171. Deitmer JW, Ellis D (1978) Changes in the intracellular sodium activity of sheep heart purkinje fibres produced by calcium and other divalent cations. The Journal of Physiology 277: 437–453.
172. Allen DG, Eisner DA, Orchard CH (1984) Factors influencing free intracellular calcium concentration in quiescent ferret ventricular muscle. The Journal of Physiology 350: 615–630.
173. Sheu S, Korth M, Lathrop D, Fozzard H (1980) Intra- and extracellular K^+ and Na^+ activities and resting membrane potential in sheep cardiac purkinje strands. Circulation Research 47: 692–700.
174. Spitzer KW, Walker JL (1980) Intracellular chloride activity in quiescent cat papillary muscle. American Journal of Physiology - Heart and Circulatory Physiology 238: H487–H493.
175. Deitmer JW, Ellis D (1980) The intracellular sodium activity of sheep heart purkinje fibres: effects of local anaesthetics and tetrodotoxin. The Journal of Physiology 300: 269–282.
176. Miura DS, Hoffman BF, Rosen MR (1977) The effect of extracellular potassium on the intracellular potassium ion activity and transmembrane

potentials of beating canine cardiac purkinje fibers. The Journal of General Physiology 69: 463–474.
177. Abete P, Vassalle M (1992) Role of intracellular Na^+ activity in the negative inotropy of strophanthidin in cardiac purkinje fibers. European Journal of Pharmacology 211: 399–409.
178. Vaughan-Jones RD (1979) Regulation of chloride in quiescent sheep-heart purkinje fibres studied using intracellular chloride and pH-sensitive micro-electrodes. J Physiol (Lond) 295: 111–137.
179. Cyran SE, Phillips J, Ditty S, Baylen BG, Cheung J, et al. (1993) Developmental differences in cardiac myocyte calcium homeostasis after steady-state potassium depolarization: Mechanisms and implications for cardioplegia. The Journal of Pediatrics 122: S77–S83.
180. Chapman RA (1986) Sodium/calcium exchange and intracellular calcium buffering in ferret myocardium: an ion-sensitive micro-electrode study. The Journal of Physiology 373: 163–179.
181. Vaughan-Jones RD (1986) An investigation of chloride-bicarbonate exchange in the sheep cardiac purkinje fibre. Journal of Physiology 379: 377–406.
182. Bountra C, Powell T, Vaughan-Jones RD (1990) Comparison of intracellular pH transients in single ventricular myocytes and isolated ventricular muscle of guinea-pig. The Journal of Physiology 424: 343–365.
183. Gambassi G, Hansford RG, Sollott SJ, Hogue BA, Lakatta EG, et al. (1993) Effects of acidosis on resting cytosolic and mitochondrial Ca^{2+} in mammalian myocardium. The Journal of General Physiology 102: 575–597.
184. Fozzard HA, Lee CO (1976) Influence of changes in external potassium and chloride ions on membrane potential and intracellular potassium ion activity in rabbit ventricular muscle. J Physiol 256: 663–689.
185. Carmeliet E, Verdonck F (1977) Reduction of potassium permeability by chloride substitution in cardiac cells. The Journal of Physiology 265: 193–206.
186. Wu M, Tsai M, Tseng Y (1994) DIDS-sensitive pH_i regulation in single rat cardiac myocytes in nominally HCO_3^- free conditions. Circulation Research 75: 123–132.
187. Bolton TB, Vaughan-Jones RD (1977) Continuous direct measurement of intracellular chloride and ph in frog skeletal muscle. The Journal of Physiology 270: 801–833.
188. Bountra C, Vaughan-Jones RD (1989) Effect of intracellular and extracellular pH on contraction in isolated, mammalian cardiac muscle. The Journal of Physiology 418: 163–187.
189. Miura D, Rosen M (1978) The effects of ouabain on the transmembrane potentials and intracellular potassium activity of canine cardiac purkinje fibers. Circulation Research 42: 333–338.